This is a **peer-reviewed manuscript version** of the article:

Piperno, L., Rasi, S., De Santis, S., Masi, A., Santoni, A., Mancini, A., Angrisani Armenio, A., Pinto, V., Farjas, J., Sotgiu, G., & Celentano, G. Elucidation of the decomposition reactions of low-fluorine YBa2Cu3O7-x precursors during film pyrolysis. *Journal of Analytical and Applied Pyrolysis*, vol. 148 (June 2020), art. 104777. DOI https://doi.org/10.1016/j.jaap.2020.104777

The Published Journal Article is available at:

https://doi.org/10.1016/j.jaap.2020.104777

© 2020. This manuscript version is made available under the CC-BY-NC-ND 4.0 license https://creativecommons.org/licenses/by-nc-nd/4.0/

Elucidation of the decomposition reactions of low-fluorine $YBa_2Cu_3O_{7-x}$ precursors during film pyrolysis

L. Piperno[1,2], S.Rasi[3,4], S. De Santis[1], A. Masi[1,2], A. Santoni[2], A. Mancini[2], A. Angrisani Armenio[2], V. Pinto[2], J. Farjas[3], G. Sotgiu[1], G. Celentano[2],

1) Roma Tre University, Engineering Department, Via Vito Volterra 62, 00146 Rome, Italy

2) ENEA Frascati Research Centre, Via Enrico Fermi 00044 Frascati, Italy

3) University of Girona, Campus Montilivi, Edif. PII, E17003 Girona, Catalonia, Spain

4) Institut de Ciència de Materials de Barcelona, ICMAB – CSIC, Campus UA Barcelona, E-08193 Bellaterra, Catalonia, Spain

ABSTRACT: Chemical solution deposition methods such as low-fluorine metal organic decomposition, are nowadays widely employed in the production of $YBa_2Cu_3O_{7-x}$ superconducting films. The investigation of the chemical reactions that convert the organic precursors into the pyrolysis product is essential for the optimization of the pyrolysis step, and, ultimately, for the comprehension of the growth process. In this work, a detailed analysis of the single-salt precursors, of the ternary precursor solution and its thermal decomposition was carried out through infrared spectroscopy (FITR), thermogravimetric analysis (TGA), evolved gas analysis (EGA), X-Ray diffraction (XRD), coupled with quench experiments, and X-Ray photoelectron spectroscopy (XPS). The combination of these techniques led to the identification of the precursors and the proposal of a reaction path for pyrolysis. More in detail, a copper/ammonia coordination compound was identified and it is the first to decompose at low temperatures via a mixed path of hydrolysis and oxidation to produce copper oxide. The decomposition of the other two precursors is superimposed at higher temperatures and it yields a mixture of BaF_2, YF_3 and $Ba_{1-x}Y_xF_{2+x}$.

Keywords: Chemical solution deposition, Low fluorine, Metal-Organic-Decomposition, Thermal analysis, YBCO

1. Introduction

Nowadays, the possibility of obtaining low-cost coated conductors for energy applications [1–3], in particular superconducting $YBa_2Cu_3O_{7-x}$ (YBCO) films has made chemical growth methods widely employed [4]. Chemical methodologies based on fluorinated precursors, such as the case of the trifluoroacetate (TFA) route introduced by Gupta et al. [5], are the most studied and known chemical solution deposition methods (CSD) [6–8]. Among these, the low-fluorine metal organic decomposition (MOD) is now one of the most widespread techniques for the preparation of YBCO films [6,9], because of the need to reduce the processing time and the release of the non-environmentally friendly hydrofluoric acid (HF) during YBCO film processing in the fluorine-based routes [6,9].

In chemical deposition routes, the thermal characterization of the precursor solution is an essential step towards the optimization and understanding of the YBCO growth process. However, while several studies can be found concerning the thermal decomposition of the single-salt precursors[10–13] with the aid of thermal analysis (TA), a detailed analysis of the reactions involved in the decomposition of the complete organic precursor solution is still lacking. Additionally, TA is normally applied to samples in the form of powders due to experimental reasons. However, it has been proven that it is essential to apply TA on films [14–16] when the goal is to optimize thermal treatments on thin layers. In fact, the thermal behaviour of films differs from that of the corresponding powder, mainly because of the slower gas and heat transport through the bulk of powders when compared to films [14,17,18]. In low-fluorine solutions, such as the one reported in this work, the real precursors in solution are expected to be a mixture of fluorinated and fluorine-free (FF) species, which can be difficult to identify since their exact nature depends on ligand exchange equilibria. Typical fluorinated precursors involve trifluoracetic salts, while common FF precursors are acetates or propionate salts. Regarding the fluorinated precursors, a few studies were carried out on the single-salt precursors (YTFA -yttrium trifluoroacetate, and BaTFA -barium trifluoroacetate) in the form of films [19,20]. Conversely, thermal analysis of fluorine-free precursors based on acetates and propionates can be found on both film [14–16] and powder form [21–23]. The aforementioned studies of the single-salt precursors, both propionate and trifluoroacetate based, will serve as reference to understand the complex

behaviour of our low-fluorine solutions, where both fluorinated and fluorine-free species of Cu, Ba and Y can be present in the initial mixture, depending on the amount and characteristics of ligand exchange.

In this work, the single metal organic precursors and the thermal behaviour of a low-fluorine MOD precursor solution is analysed via Fourier transformed infrared spectroscopy, (FTIR) thermogravimetric analysis (TGA), evolved gas analysis (EGA), X-Ray diffraction (XRD), coupled with quench experiments, and X-Ray photoelectron spectroscopy (XPS). The different outcomes were combined to create a clearer picture of the decomposition pattern of the solution.

2. Materials and Methods

Materials

The low-fluorine YBCO precursor solution was prepared as in [24] starting from barium trifluoroacetate (Alfa Aesar, $Ba(OOCCF_3)_2 \bullet xH_2O$), yttrium acetate (Sigma Aldrich, Yttrium(III)Acetate hydrate 99.9%, $Y(CH_3CO_2)_3 \cdot xH_2O$) and copper acetate (Sigma Aldrich, Copper(II)Acetate 99.99%, $Cu(CO_2CH_3)_2$) as precursor salts. The salts were separately dissolved in a mixture of methanol and propionic acid, with the addition of a small amount of NH_3 (0.3 ml, 28-30% in water) in the solution of copper acetate to help its solubilization. The three solutions were combined and a rotary evaporation step followed, to eliminate methanol and water. After this step, the obtained solution contains only propionic acid as solvent.

Films for thermal analysis experiments were prepared by both spin coating and drop casting. The solution was deposited on 10x10 mm $LaAlO_3$ (LAO) substrates. In the case of spin coated films, 0.6 mg/LAO of sample were deposited with a single deposition and 3.57 mg/LAO with multiple sequential depositions. By drop casting a deposited mass of 12 mg was obtained. The films were dried at 70 °C for 120 mins on a hotplate. The drop-cast film was dried at 70 °C until a thick gel was obtained. The nominal film thickness (h) was calculated with the following formula $h = m/q \bullet A$ where m is the final mass of the oxides/oxifluorides after decomposition, q is the particle density and A is the substrate area. Given the complexity of the final phases, the nominal thickness is only indicative for comparison purposes among our films. Three regimes were considered in the thermal analysis of this work: very thin films (< 1μm, obtained by spin coating, sample A), intermediate thickness (around 2.5 μm, obtained via multiple spin coatings, sample B) and 8 μm (obtained by drop casting, sample C).

Methods

Thermogravimetric (TGA) and differential scanning calorimetric (DSC) analyses were carried out with a TGA/DSC1 model thermobalance by Mettler Toledo, with heating rates of 5 °C/min in an atmosphere of humid O_2 (3% water obtained by bubbling the gas through a water flask, at atmospheric pressure and 25 °C [25]), with gas flows of 60 ml/min. A 15 ml/min flow of dry air was used as protective gas for the thermobalance.

Thermogravimetric analysis coupled to evolved gas analysis (EGA) with infrared detection (TG-FTIR) was performed by connecting the gas outlet of the TG equipment to the FTIR analyzer with a steel tube kept at 200 °C, in order to prevent the condensation of the volatiles. The FTIR analyzer was equipped with a gas cell, model ALPHA II Bruker alpha, also kept at 200 °C during the experiment. Spectra of the gaseous products were recorded with a 4 cm^{-1} resolution and 30s/spectrum, in the 4000-500 cm^{-1}. For the assignment of the vibrational absorption peaks, the experimental results were compared to standard reference spectra database in the gas phase [26], when available, or from data taken from the literature [10,11]. The experimental spectra were acquired after a blank spectrum was recorded with only the humid gas flowing in the cell. The deconvolution procedure of the DTG was performed using the Fityk software [27]. The curve was fitted using Fraser-Suzuki functions [28].

X-Ray Diffraction (XRD) measurements of the powder were performed using a Rigaku SmartLab 9 kW diffractometer equipped with a rotating anode Cu tube and providing a monochromatic $K_{\alpha 1}$ radiation. The θ-2θ scans were acquired using a parallel beam geometry. The films were analysed in grazing incidence geometry with a Bruker-AXS, model A25 D8 Discover. The diffractometer was equipped with a LinxEye XE-T detector (High-Resolution Position Sensitive Detector with Energy Resolution), with standard conditions of 40 KV and 40 mA, and an X-ray tube KFL CU 2K ($\lambda_{(CuKa)}$ = 1.541840 Å).

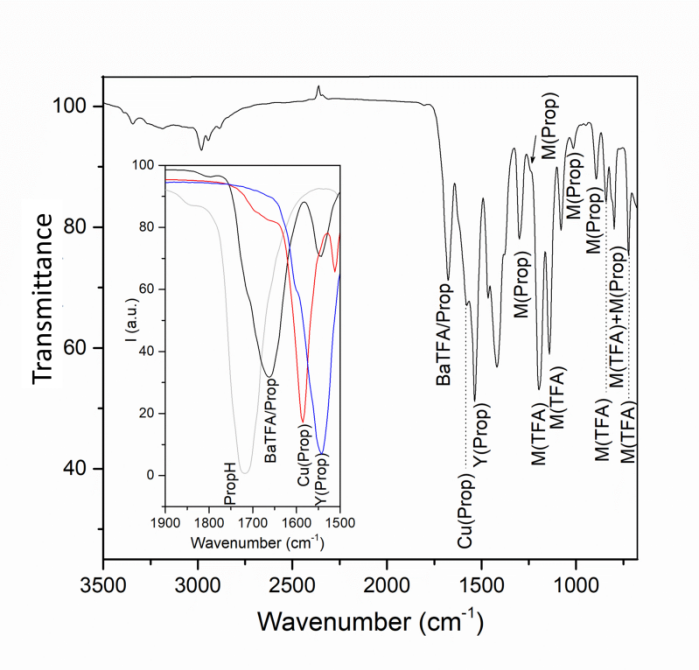

Fig. 1. FTIR spectrum of the precursor solution. The main signals were indexed by comparison with reference spectra. The inset highlights the carbonyl peaks of the involved species showing appreciable difference in the absorption frequency.

FTIR measurements were performed using a Nicolet iN10 infrared microscope (Thermo Scientific, USA) with MCT (mercury-cadmium telluride) nitrogen cooled detector and Ominc Picta workstation. Data were collected in transmission (solutions) or ATR (powders) mode in the 4000-650 cm^{-1} spectral range collecting 64 interferograms with a 8 cm^{-1} resolution. For the assignment of the vibrational absorption peaks, the experimental results were compared to standard reference spectra in the condensed phase [26], or from data taken from the literature [14,15].

Two samples were analysed via XPS, a film and a powder obtained from the TA treatment of a drop-cast sample. The film was analysed with an AlK_a non-monochromatized X-ray source. The pyrolyzed powder was dispersed onto a carbon tape substrate and analysed with a monochromatized Al K_a X-Ray beam. Calibration was done by setting the C1s binding energy to 284.6 eV. A Shirley or linear background was subtracted from the data. The binding energy is referred to the Fermi level. The error on the peak position was estimated to be ± 0.1 eV.

3. Results

Characterization of the single-salt precursors. XRD diffraction and FTIR spectroscopy were employed in the study of the precursor salts: copper acetate, yttrium acetate and barium trifluoroacetate ($CuAc_2$, YAc_3 and BaTFA respectively). First, the spectra of the commercial salts were recorded. Then, the salts were dissolved, separately, in propionic acid to simulate the environment they would encounter in the solution. In order to maximize the signal of the dissolved chemical species with respect to that of the solvent, evaporation of as much propionic acid as possible was carried out on a hotplate at 80 °C (it was necessary to increase the temperature up to 140 °C for the Ba precursor). Significant reduction of the volume was obtained after 24 h on the hotplate, and cooling of the solutions led to the precipitation of some salts. The precipitates were collected, dried and analysed. From the FTIR and XRD analysis of the single-salt precipitates (reported in the supporting material) it was possible to identify copper propionate, $CuProp_2$, yttrium propionate, $YProp_3$, $BaTFA_2$ and a mixed species defined barium trifluoroacetate/propionate, BaTFA(Prop), as the effective precursors. This is not surprising since ligand exchange with the solvent is known to happen in the solution [7,29].

Characterization of the precursor solution. The IR measurement of the solution was performed, like in the case of the precursors, on a gel obtained by keeping the solution on a hotplate at 80°C for several hours. After treatment, a blue glass-like layer was obtained, that was ground and reduced to powder before analysis. Due to this texture, the analysis was performed in the ATR mode. The IR spectrum of the gel is shown in Fig. 1. The broad band visible above 3000 cm^{-1} is likely due to the O-H stretching of adsorbed water, whereas at 3000 cm^{-1} the peaks relative to the C-H stretching are present. In the fingerprint region, accurate attribution of the peaks to single species is not possible; however, by comparison with the precursors' spectra, it is possible to discern the contribution of the trifluoroacetate and propionate moieties, as labelled in Fig. 1. The carbonyl region, instead, shows more resolved peaks. Given the distance among the C=O stretching of the different chemical compounds,

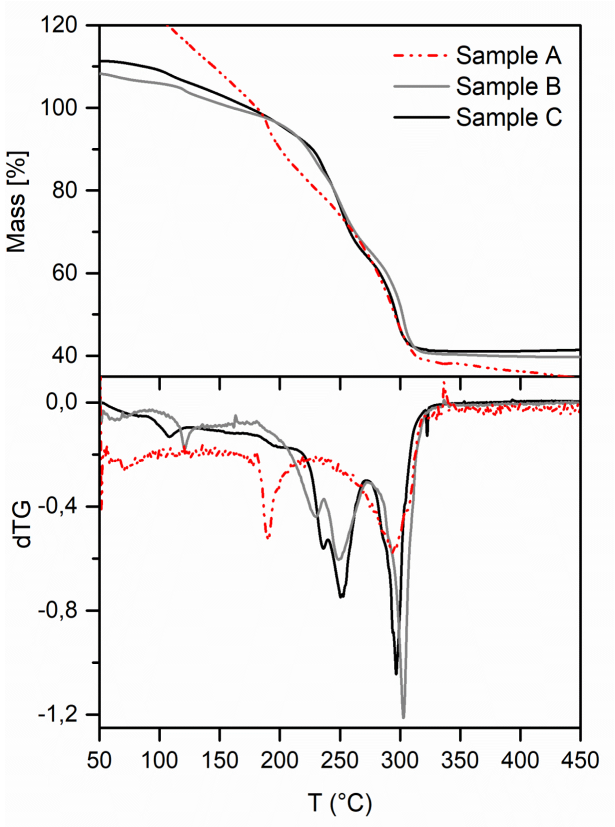

Fig. 2. TG and dTG curves of the analysed samples. The samples differ in nominal thickness: In red (dashed) the 0.6 µm sample A, in gray the 2.5 µm sample B and in black the 8 µm sample C. The 100% mass refers to the dry proposed precursors.

highlighted in the inset, the comparison of the pattern obtained for the ternary solution of the precursors with the pattern obtained for the isolated compounds allows identification of the single species. Therefore, from the spectrum it is possible to identify $CuProp_2$, $YProp_3$, $BaTFA_2$ and the barium mixed compound referred to as BaTFA(Prop). This identification does not exclude however the presence of minor amounts of additional species that might be hidden by these principal absorption bands.

Thermogravimetric analysis of the solution. Typically, when the main solvent has a high boiling point, the first part of the TG profile is strongly influenced by the mass loss due to solvent evaporation. As shown in Fig. 2, the TG and dTG profile for the film spinned in the standard conditions [24] (sample A, nominal thickness h < 1 µm) shows a relatively broad mass loss up to approximately 300 °C, with two main decomposition steps evident from the DTG curve. It is worth noting that, in these conditions, the sample mass is relatively close to the detection limit of the instrument. In order to be able to evaluate the decomposition paths with more clarity, this analysis was compared to two other measurements, performed on thicker samples (sample B, h = 2.5 µm and sample C, h > 8 µm), and therefore characterized by a higher amount of deposited material. The TG analysis was performed in the same aforementioned conditions: in these cases, thanks to the higher mass amount and to a lesser relative solvent evaporation, the various steps of the decomposition are clearer. Apart from the slow decrease of the mass most likely due to solvent evaporation between 50 and 150 °C, two main steps can be identified. The first significant mass loss, between 150-260°C is due to the superposition of at least two less resolved steps, as evidenced by the two peak contributions in the dTG curve. In the case of the second main mass loss step, a shoulder on the low temperature side of the relative peak suggests, also in this case, that decomposition of multiple species is taking place in different stages. The DSC signal consists of exothermic peaks, as expected for the thermal decomposition in oxidative atmospheres (as shown in the supporting material).

The similarities observed in the curves of samples characterized by different thickness suggests that their decomposition paths are similar. In fact, a shift in decomposition temperature (onset and final) is normally observed upon changes in film thickness, while a completely different reaction path is often observed when switching from films to powders. It is known from the literature that decomposition processes can differ greatly when the species are decomposed in the form of films with respect to the powders decomposed in crucibles,

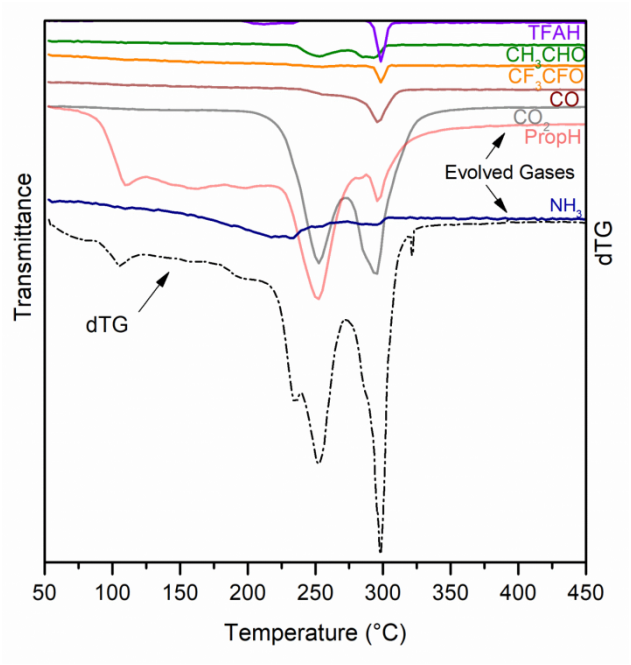

Fig. 3. Superposition of the TG curve of Sample **C** and the results of the EGA analysis. The evolution curves of the gaseous species were extrapolated by plotting a characteristic transmission frequency for each volatile versus temperature.

because the greater aspect ratio in films results in faster gas transport when compared to the slow transport in the bulk of powders [14,17,18].

Evolved Gas Analysis via Infrared Spectroscopy. Infrared spectroscopy was employed to obtain information on the volatiles produced by the thermal decomposition of sample C. Relatively large quantities of deposited material are necessary to obtain clear signals in the gas analysis, and for this reason two films were decomposed instead of one for the TG-FTIR experiment. The original spectra obtained from the EGA analysis are shown in the supporting material, while the temperature-resolved evolution curves of the volatiles are reported in fig 3. These curves were extrapolated by plotting the intensities at the respective transmission frequencies versus temperature. The first thing to stress is that certain peaks are always visible: these were attributed to the solvent, propionic acid (PropH), continuously evolving from the film, and CO_2 from atmospheric contamination. The first event is observed between 150 °C and 250 °C, with the highest intensity at 230 °C: in this temperature range, two separate signals appear at 965 cm^{-1} and 929 cm^{-1} that are compatible with the two strongest peaks of the ammonia reference spectrum. Right after the disappearance of the ammonia signals, in the temperature range between 225 °C and 275 °C, strong evolution of propionic acid and CO_2 is observed, along with the appearance of IR signals belonging to a new molecule, acetaldehyde (identified by the characteristic peaks at 2735 cm^{-1}). These three species are compatible with the decomposition process of metal propionates. Very small amounts of CO are also detected in the evolved gases around 260 °C. The last mass loss stage, that occurs between 260 °C and 350 °C, causes the evolution of new species, along with smaller amounts of propionic acid and acetaldehyde. These new signals are attributed to CF_3CFO (1892 cm^{-1}), CF_3COOH (trifluoroacetic acid, TFAH, at 1211 and 1195 cm^{-1}) which are, together with CO, products of the decomposition of metal trifluoroacetates. Above 350 °C, no evolution of gases is visible, meaning that the organic decomposition reactions are completed before this temperature.

XRD Analysis of the solid residue. X-ray analysis was performed to evaluate the crystalline structure of the products forming at different temperatures. For the scope, four samples were prepared according to the standard spinning procedure mentioned above (i.e. nominal thickness inferior to 1 µm) and heated in the condition used for the TGA experiments up to 230, 260 and 300 °C respectively, and then quenched. In Fig. 4, the XRD diffractograms of the samples are reported in comparison with the pattern obtained from sample A at 500 °C and the powder recovered from sample C at 500 °C. Starting from the lower temperatures, the 230 °C and 260 °C samples are characterized by the presence of a broad amorphous band at low 2θ values and by two broad peaks at 2θ= 35.5° and 2θ= 38.7° which are attributed to the (-111) and (111) reflection of CuO. The two small peaks at 2θ=

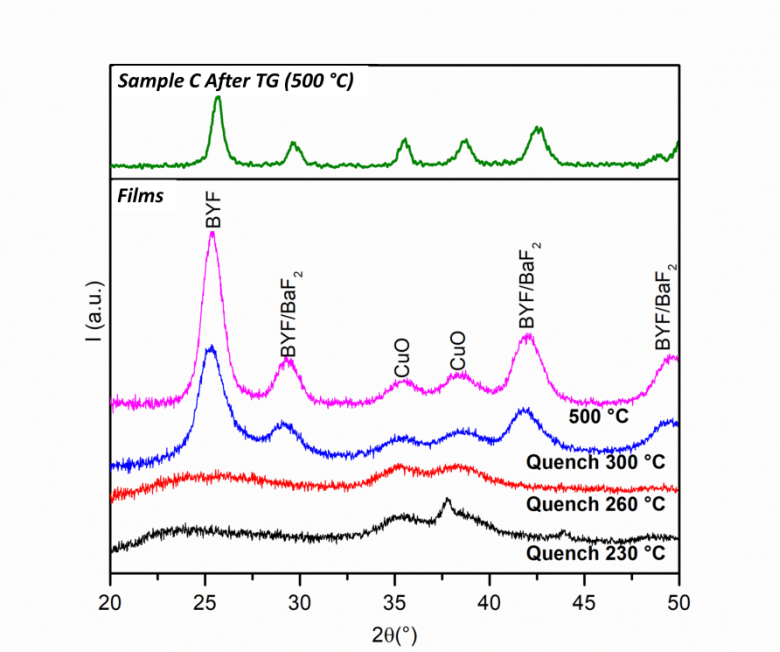

Fig. 4. XRD spectra of the three quenched films and sample A (lower panel), and of the powder obtained from the TA of sample C (upper panel)

37.8 and 2θ= 43.9 in the 230 °C sample, much sharper than the CuO, are residual signals from the substrate. The situation pictured by the quenched sample at 260 °C is identical: only CuO can be detected from the diffraction pattern, and the intensity of the peaks is not increased with respect to the 230 °C spectrum. At 300 °C instead, other peaks appear attributable to BaF_2 or to the solid solution of YF_3 in BaF_2 (BYF). At higher temperatures (500°C), crystallinity improves without differences in the pattern apart from a small shift of the BaF_2 diffraction peaks, likely due to a different amount of Y dissolved in BaF_2, leading to the deformation of its fluoride structure [30].
Regarding the powder obtained from sample C, the reason for analyzing it was to obtain information without the interference of the substrate, and to understand if the increased thickness of the deposited layer has some effect on the final product. The compounds identified in the XRD diffraction pattern of the fully pyrolyzed film (sample A, Fig.4) are the same as the corresponding powder (sample C, Fig.4). However, a small difference can be detected in the position of the BYF peaks. As already mentioned, the position of the peak is correlated with the quantity of Y that has diffused into the BaF_2 structure [30]. It is possible, by calculating the lattice parameter of the BYF structure, to derive the stoichiometry of the compound. It is known that the lattice parameter of BYF comes from a linear combination of the cubic BaF_2 and YF_3 structures [31], therefore, once the BYF lattice spacing is extracted from the 2θ position through the Bragg's formula, it can provide an estimation of the composition of BYF. In the case of the fully pyrolyzed film the calculation gives $Ba_{0.88}Y_{0.22}F_{2.22}$ whereas for the powder we found $Ba_{0.65}Y_{0.35}F_{2.35}$. This difference is consistent with the different extent of the BYF decomposition reaction to yield separate oxides and oxyfluoride species ($2YF_{3(BYF\ Soln)} + H_2O \rightarrow Y_2O_3+6HF$ or $YF_{3(BYF\ Soln)} + H_2O \rightarrow Y(OH)_3+3HF$, [32]) as a function of film thickness; in fact, like other solid-gas reactions, this reaction is affected by gas transport, in particular water diffusion into the sample and HF outdiffusion. The thicker the film (sample C), the more the equilibrium is shifted towards reactants.

X-Ray Photoelectron Spectroscopy. The same quenched film (T_{quench}=230 °C) and powder obtained from sample C were analysed by XPS spectroscopy. Particular attention was paid to the signals of the 1s orbital for F, 3d orbitals of Y and Ba, the 2p orbitals of Cu (shown in Fig. 5), and the 1s orbital for carbon (Fig. 6). The analysis was first performed on the powder obtained from sample C whose composition was already partially known, due to the abundance of previous studies. The XPS analysis performed on sample C, is in agreement with the XRD results of Fig.4, that show the presence of CuO and BYF. Regarding the F signal, the 1s peak can be successfully fit with two components with 1.7 FWHM, whose binding energy (BE) values are perfectly matched to those of YF_3 at 684.8 eV and BaF_2 at 683.8 eV [33]. We can assume that the F1s line is given by the superposition of two components, one related to a F-Ba bond and one to a F-Y bond. Also, the analysis of Ba3d and Y3d reveal binding energies very close to those of YF_3 and BaF_2 [34,35], we can therefore conclude that these species are present in the sample

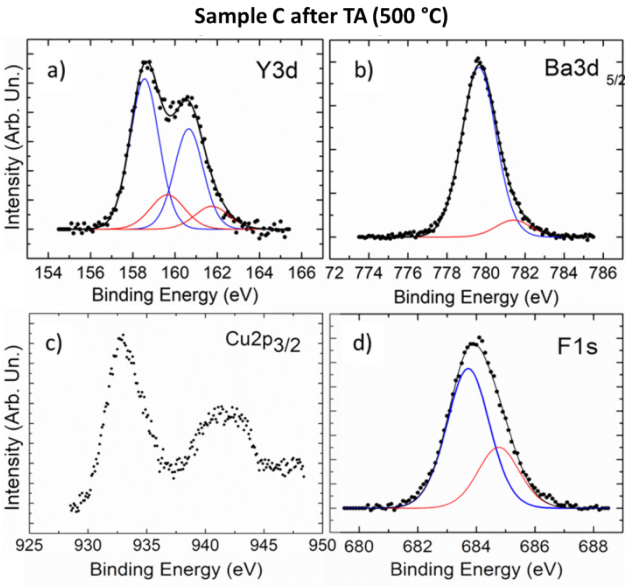

Fig. 5. XPS spectra of the relevant orbital signals analyzed in sample C after TA a) Y3d b) Ba3d5/2, c) Cu2p3/2 and d) F1s.

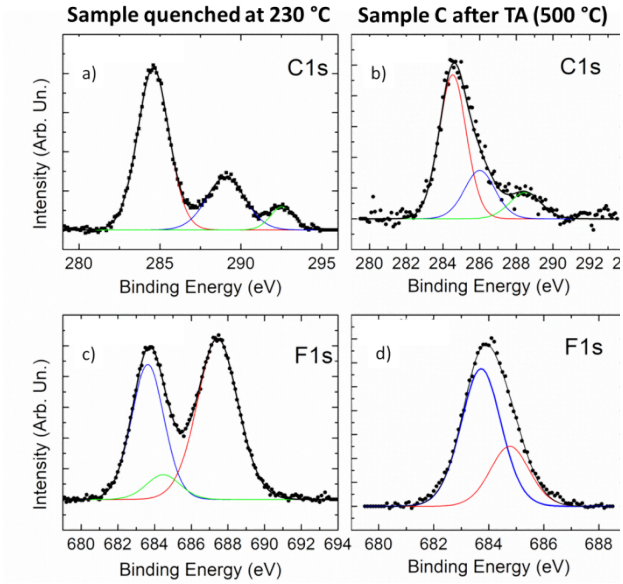

Fig. 6. XPS spectra of the relevant orbital signals analyzed in the quenched sample a) C1s and c) F1s, and in sample C after TA b) C1s and d) F1s.

treated up to 500 °C. The XPS analysis, being very sensitive, also reveal other minor components. Both Y and Ba signals show small components at higher binding energies that are compatible with mixed species like Ba-OH-F or Y-OH-F. The hydroxylation of surfaces is not surprising since the samples are kept in air, but also the presence of $Y(OH)_3$, YOF and barium oxifluoride in the pyrolyzed sample is known to occur in literature [30–32]. Since this satellite peaks could be interpreted either way, a clear match can't be made. As regards copper, from the intensity of the satellite peak it would seem that copper is in the Cu^{2+} state. The $Cu2p_{3/2}$ peak position at 932.9 eV is in agreement with literature data for CuO as supported by several authors [36–40]. As regards the visible peak broadening, a possible explanation for this could be the presence of a mixture of CuO and $Cu(OH)_2$ [37,38] which would explain the widening of the peak at higher BE. Alternatively, Cu_2O could be responsible even though the reduction of copper is not likely to happen in an oxidizing atmosphere. The one hypothesis that can be discarded for sure is the presence of any Cu-F bond: CuF_2 is excluded as there is no intensity at 936.3eV, the reference value for this compound. The C1s core-level shown in Fig. 6 is clearly free from components due to C-F bonding which appear at about 292 eV [35]. The main component at 284.6 eV is due to C-C, C-H bonds. The component at 286.1 eV is due to C-OH species and the last one at 288.6 eV to C=O bonds or to residual COO-R groups although they were shown to appear above 289eV. The presence of signals related to organic moieties in the pyrolyzed powder can be due to an incomplete decomposition of the multiply deposited layers of the sample.

For the sample at 230 °C the scenario remains basically unchanged, confirming the XRD analysis. The main difference compared to samples decomposed to 500 °C is in the F and C 1s signals, whose comparison is shown in Fig. 6. As regards F, the presence of a very intense peak of the F1s signal is observed at 687.9 eV that is related to the $-CF_3$ moiety of the trifluoroacetate molecule [35]. The presence of this signal is consistent with an incomplete reaction of the trifluoroacetate precursors, as expected at 230 °C. This could not be appreciated by XRD analysis alone. Additionally, the C1s signals shows differences with respect to the sample treated up to 500 °C: the C-F component is now visible at 292.5 eV, together with the C-C and C-H components also observed, with lower intensities, in the 500 °C sample. Furthermore, the components related to YF_3 and BaF_2 both in the F1s, Y3d and Ba3d signals are already visible, meaning that the formation of the final products already begins at 230 °C. The interesting information is that no Y_2O_3 or any other Y-O compound is visible in the quenched sample, even though they are known products of $Y(Prop)_3$ decomposition. This could either mean that they do not form at all, or that they are formed but immediately converted in YF_3 and they cannot be detected.

Deconvolution of the dTG curve. In order to perform a more quantitative analysis of the thermogravimetric data, deconvolution of the dTG curve of sample C was carried out, and is reported in Fig. 7. The initial mass was calculated with respect to the final composition derived by the other analyses. The area below the peaks can be directly correlated with the mass loss of the sample. The percentage of each mass loss peak with respect to the total

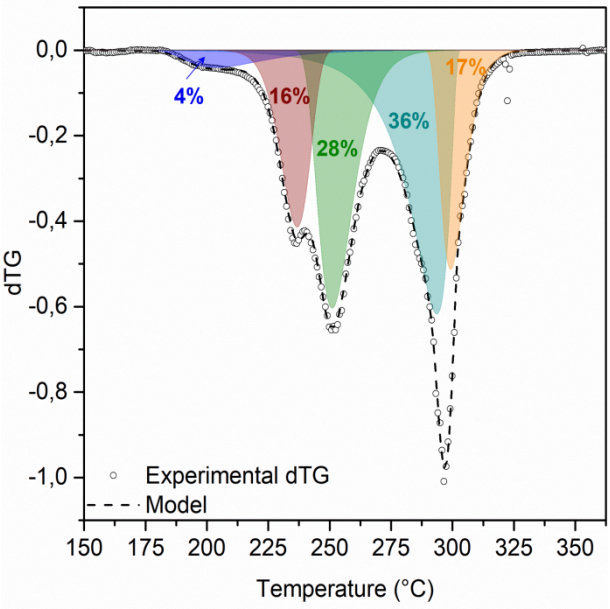

Fig. 7. Deconvolution of the dTG curve for sample C. The mass loss percentages of the single reactions are shown for each peak.

mass loss, can help to identify the chemical species that are decomposing during each step.

The first step of the dTG can be fitted with only two peaks that together make up for around 48% of the total mass loss. This percentage is compatible with the decomposition of a copper/ammonium compound to copper oxide. The presence of this compound is considered in consequence of the results of the EGA analysis. Thus, the reactions involved in the first step could be

$$3Cu(Prop)_2NH_3 \rightarrow 3Cu(Prop)_2 \quad (\Delta m=5\%\ \Delta m_{tot}), \text{ and}$$

$$3Cu(Prop)_2 \rightarrow 3CuO \quad (\Delta m=42\%\ \Delta m_{tot})$$

The second step of the dTG curve, as suggested by EGA, is related to the decomposition of the fluorinated species, in particular BaTFA, BaTFA(Prop) and yttrium propionate. An accurate representation of the data is obtained assuming the presence of three peaks below the experimental curve. The sum of the areas of these peaks give a total of 52% of the total mass loss that is what we expect from the full decomposition of $YProp_3$ and BaTFA. More in detail, the deconvolution identifies three processes, whose mass loss is compatible with the following reactions:

$$2Ba(TFA)_2 \rightarrow 2BaF_2\ (\Delta m= 38\%\ \Delta m_{tot})$$

$$Y(Prop)_3 \rightarrow YF_3 \quad (\Delta m= 17\%\ \Delta m_{tot})$$

The decomposition of the mixed species BaTFA(Prop), whose presence was inferred by FITR analyses, was not taken into consideration because the difference in the mass loss between the reaction of only BaTFA or xBaTFA+(2-x)BaTFA(Prop) to BaF_2 is negligible at this level of approximation. This reaction path is, of course, oversimplified since both reactions are known to happen through different mechanisms also involving competing reactions (see next sections).

4. Discussion

The combination of the results obtained via the different techniques can be combined to draw a clearer picture of the pyrolysis decomposition mechanism. First of all, the precursor analysis confirmed the metal propionates to be the real precursors in the decomposition reactions, due to the ligand exchange with the solvent in excess, which is expected to take place and is in agreement with [29]. Therefore, the calculation of the mass loss steps in the TG analysis was obtained considering propionates and mixed ligands precursors, and the complementary TA techniques used confirmed that the thermal behaviour is in agreement with that already reported for the single precursor salts.

Coupling the TG with the EGA analysis, the evolution of gaseous products can be localized in three narrow temperature ranges, which are in agreement with the decomposition of the copper precursor in the first stage, and with the decomposition of $YProp_3$ and the barium species in the second stage. In the first range, detection of ammonia is not surprising because, as explained in the experimental section, ammonium hydroxide is used during the preparation of the solution to help the solubilization of copper acetate. The evolution of ammonia at this high temperature, considering the high volatility of the substance, can be explained with the possible coordination of the ammonium ion with the organic anions present in the solution. Simple ammonium compounds such as ammonium acetate or ammonium propionate have a lower boiling point (117 °C and 142 °C, respectively), compared to the temperatures considered here, therefore strong coordination to a metallic ion is proposed. In fact, the existence of copper superstructures known as *paddlewheels* is known, in which copper-ligand dimers accept an additional dative bond from species having a free lone pair, such as ammonia or water, in their empty apical positions [41]. Therefore it is adequate to suppose that similar species are present in the solution. This coordination compound starts to decompose around 150 °C, yielding gaseous ammonia as a product.

Right after the decrease of the ammonia signals, in the temperature range between 225 °C and 275 °C, copper propionate decomposes to CuO: strong evolution of propionic acid and CO_2 is observed, along with the appearance of IR signals belonging to acetaldehyde. These three species are compatible with the decomposition through hydrolysis, that causes the production of large amounts of propionic acid, and through oxidation, that produces CO_2, acetaldehyde, propionic acid and water. Considering also the information obtained via XRD on the appearance of CuO at low temperatures, this second temperature range involves the complete conversion of copper propionate to CuO. It is interesting for chemical deposition methodologies to discuss this intermediate temperature range, at 260 °C, where we can notice the effect of film thickness. In Fig. 2, the dTG curve of sample A is presented together with those of sample B and C. It can be observed that the first step of the process is shifted to lower temperatures for sample A. If we suppose that the first step is related to the decomposition of $CuProp_2$ alone, as indicated by the XRD and EGA analysis, we can explain this shift with $CuProp_2$ degradation via the hydrolysis reaction path [15], which instead does not affect as much the yttrium and barium salts. Just like observed for $CuProp_2$ alone, also in our ternary solution it can be expected that for the thinnest film the hydrolysis path is favoured with respect to the oxidation path that occurs at higher temperature [15]. Conversely, the decomposition of the other species is less influenced by the thickness of the film and occurs in the same T range for samples A, B and C.

The second mass loss stage (between 260 °C and 350 °C), causes CF_3CFO, CF_3COOH and CO evolution, that are known products of the decomposition of metal trifluoroacetates. Therefore, we can infer that in this third stage the decomposition of the majority of the metal trifluoroacetates takes place. Also, the decomposition of some residual propionate responsible for the evolution of acetaldehyde occurs. If we suppose that copper propionate has already decomposed, the remaining species to decompose are BaTFA(Prop), $YProp_3$ and BaTFA. The mixed ligands precursor was considered in order to take into account the results of the FTIR analysis of the precursor and the EGA results, that shows evolution of propionate decomposition byproducts in the second mass loss stage. The hypothesis of the barium and yttrium precursors decomposing at this temperature, together with the proposed intermediate BaF(TFA), is consistent with data from the literature [11,14,42] and with the rest of the performed analysis. In fact, the mass losses calculated for these reactions are in agreement with those obtained from the dTG deconvolution. $Y(Prop)_3$ decomposition occurs in presence of highly reactive fluorinated species that lead to direct formation of the YF_3 [43,44], without any detectable intermediate.

The expected final compounds CuO, YF_3, BaF_2 and BYF already appear at 300 °C in the XRD spectrum of the quenched sample and the decomposition process of the YBCO precursors is complete before 350°C. A significant piece of information is that the final compositions of the films characterized by different thicknesses, as detected by XRD, are the same. This suggests that the mechanism of the decomposition remains the same, with only minor

differences in the stoichiometry of the BYF compound. Again, no signal relative to the other possible secondary phases (Y_2O_3, $BaCO_3$ or Cu_2O) is detected, apart from the minor contribution due to atmospheric contamination.

Summing up all the information obtained through the performed analyses and starting from this solution composition

$$3CuProp_2NH_3+YProp_3+BaTFA(Prop)+BaTFA_2$$

we can propose the following reaction paths for the thermal decomposition of our low-fluorine solution.

The proposed steps are the following:

150-210°C: Cu/NH_3 coordination compounds decomposition

$$3CuProp_2NH_3 \rightarrow 3CuProp_2 + 3NH_3$$

210-260°C: Copper propionate hydrolysis and oxidation

$$3CuProp_2+3H_2O \rightarrow 3CuO+ 6PropH$$

$$3CuProp_2+12O_2 \rightarrow 3CuO+ 3PropH + 3CH_3CHO + 3CO_2$$

260-250°C: Yttrium propionate, barium trifluoroacetate and barium trifluoroacetate/propionate multistep decomposition. For BaTFA we have different reactions that compete towards the formation of BaF_2.

$$2Ba(TFA)_2 \rightarrow 2{:}CF_2+2CO_2+2BaF(TFA)$$

$$\textit{1} \quad \begin{cases} :CF_2+H_2O \rightarrow 2HF+CO \\ :CF_2+HF+CO_2 \rightarrow CF_3COOH \end{cases}$$

$$\textit{2} \quad 2BaF(TFA) + 2{:}CF_2 \rightarrow 2CF_3CFO+2CO+2BaF_2$$

$$\textit{3} \quad 2BaF(TFA) \rightarrow 2{:}CF_2+2CO_2+2BaF_2$$

For the mixed species we propose a decomposition through oxidation of the propionate moiety to give the intermediate BaF(TFA) that then decomposes to BaF_2 according to reactions 2 and/or 3.

$$2BaTFA(Prop)+5/2O_2+{:}CF_2 \rightarrow 2CH_3CHO+3CO_2+ H_2O+2BaF(TFA)$$

For yttrium propionate decomposition we propose a direct conversion of $YProp_3$ to YF_3, any oxide intermediate is supposed to react promptly either with the HF or the $:CF_2$ produced by the BaTFA decomposition as proposed in [19,45].

$$2YProp_3 + 3O_2 + 6HF \rightarrow 2YF_3 + 3PropH + 3CH_3CHO + 3CO_2 + 3H_2O$$

This reaction path was developed for thick films, but it was already discussed that the main difference between thick and thin films is the preferred hydrolysis process for $CuProp_2$ decomposition. We can therefore assume that that the reaction path are the same, even if shifted to slightly different temperatures.

5. Conclusions

In this work we have provided thorough analysis of the precursor solution of YBCO films obtained via low-fluorine MOD, together with characterization of the single salt precursor. We have demonstrated that the real precursors for YBCO are the propionates of the metals that form in the solution due to ligand exchange, and that in the case of Ba a mixed TFA/propionate species is formed. We have analysed in detail the decomposition behaviour of the solution, in conditions as close as possible to the ones used for thin film synthesis in order to extricate the different reactions involving the single precursors. This analysis was supported with other techniques that were employed to identify the composition of the film at certain fundamental moments of the decomposition process.

This combination of analyses gave us the chance to propose a reaction path for the decomposition of YBCO precursor during the pyrolysis step.

Acknowledgments

This work has been carried out within the framework of theEUROfusion Consortium and has received funding from the EURATOM programme 2014–2018 and 2019-2020 under grant agreement N° 633053. The views and opinions expressed herein do not necessarily reflect those of the European Commission. This work was also supported by Ministerio de Ciencia, Innovación y Universidades (grant number RTI2018-095853-B-C22), by the Center of Excellence Severo Ochoa (SEV-2015-0496), the Generalitat de Catalunya (2017-SGR-1519) and the Universitat de Girona (UdG, contract number MPCUdG2016/059).

References

[1] H. Maeda, Y.Y.-I.T. on Applied, undefined 2013, Recent developments in high-temperature superconducting magnet technology, IEEE TAS, 24(3) (2013) 1-12.

[2] M. Atikur Rahman, A Review on Cuprate Based Superconducting Materials Including Characteristics and Applications, Am. J. Phys. Appl. 3 (2015) 39. doi:10.11648/j.ajpa.20150302.15.

[3] X. Obradors, T. Puig, Coated conductors for power applications: materials challenges, Supercond. Sci. Technol. 27 (2014) 44003.

[4] B.A. Albiss, I.M. Obaidat, Applications of YBCO-coated conductors: a focus on the chemical solution deposition method, J. Mater. Chem. 20 (2010) 1836–1845.

[5] A. Gupta, R. Jagannathan, E.I. Cooper, E.A. Giess, J.I. Landman, B.W. Hussey, Superconducting oxide films with high transition temperature prepared from metal trifluoroacetate precursors, Appl. Phys. Lett. 52 (1988) 2077–2079.

[6] T. Araki, I. Hirabayashi, Review of a chemical approach to \ch{YBa2Cu3O$_{7-x}$}-coated superconductors—metalorganic deposition using trifluoroacetates, Supercond. Sci. Technol. 16 (2003) R71.

[7] T. Schneller, R. Waser, M. Kosec, D. Payne, Chemical solution deposition of functional oxide thin films, Springer, 2013.

[8] R.W. Schwartz, T. Schneller, R. Waser, Chemical solution deposition of electronic oxide films, Comptes Rendus Chim. 7 (2004) 433–461.

[9] L. Ciontea, A. Angrisani, G. Celentano, T. Petrisor Jr, A. Rufoloni, A. Vannozzi, A. Augieri, V. Galuzzi, A. Mancini, T. Petrisor, Metal propionate synthesis of epitaxial \ch{YBa2Cu3O$_{7-x}$} films, in: J. Phys. Conf. Ser., 2008: p. 12302.

[10] M. Mosiadz, K.L. Juda, S.C. Hopkins, J. Soloducho, B.A. Glowacki, An in-depth in situ IR study of the thermal decomposition of copper trifluoroacetate hydrate, J. Fluor. Chem. 135 (2012) 59–67.

[11] M. Mosiadz, K.L. Juda, S.C. Hopkins, J. Soloducho, B.A. Glowacki, An in-depth in situ IR study of the thermal decomposition of yttrium trifluoroacetate hydrate, J. Therm. Anal. Calorim. 107 (2011) 681–691.

[12] M. Mosiadz, K.L. Juda, S.C. Hopkins, J. Soloducho, B.A. Glowacki, An in-depth in situ IR study of the thermal decomposition of barium trifluoroacetate hydrate, Thermochim. Acta. 513 (2011) 33–37.

[13] X. Palmer, C. Pop, H. Eloussifi, B. Villarejo, P. Roura, J. Farjas, A. Calleja, A. Palau, X. Obradors, T. Puig, others, Solution design for low-fluorine trifluoroacetate route to \ch{YBa2Cu3O$_{7-x}$} films, Supercond. Sci. Technol. 29 (2015) 24002.

[14] S. Rasi, S. Ricart, X. Obradors, T. Puig, P. Roura, J. Farjas, Thermal decomposition of yttrium propionate: film and powder, J. Anal. Appl. Pyrolysis. 133 (2018) 225–233.

[15] S. Rasi, F. Silveri, S. Ricart, X. Obradors, T. Puig, P. Roura-Grabulosa, J. Farjas, Thermal decomposition of CuProp2:

In-situ analysis of film and powder pyrolysis, J. Anal. Appl. Pyrolysis. 140 (2019) 312–320.

[16] S. Rasi, S. Ricart, X. Obradors, T. Puig, P. Roura-Grabulosa, J. Farjas, Radical and oxidative pathways in the pyrolysis of a barium propionate-acetate salt, J. Anal. Appl. Pyrolysis. (2019) 104640.

[17] J. Farjas, D. Sanchez-Rodriguez, H. Eloussifi, R.C. Hidalgo, P. Roura, S. Ricart, T. Puig, X. Obradors, Can We Trust on the Thermal Analysis of Metal Organic Powders for thin film preparation?, MRS Proc. 1449 (2012) mrss12-1449-bb01-09. doi:10.1557/opl.2012.919.

[18] P. Roura, J. Farjas, S. Ricart, M. Aklalouch, R.G.-T.S. Films, undefined 2012, Synthesis of nanocrystalline ceria thin films by low-temperature thermal decomposition of Ce-propionate, Elsevier. (n.d.). https://www.sciencedirect.com/science/article/pii/S0040609011017068 (accessed September 17, 2019).

[19] J. Farjas, J. Camps, P. Roura, S. Ricart, T. Puig, X. Obradors, The thermal decomposition of barium trifluoroacetate, Thermochim. Acta. 544 (2012) 77–83.

[20] H. Eloussifi, J. Farjas, P. Roura, J. Camps, M. Dammak, S. Ricart, T. Puig, X. Obradors, Evolution of yttrium trifluoroacetate during thermal decomposition, J. Therm. Anal. Calorim. 108 (2012) 589–596.

[21] J.-C. Grivel, Thermal decomposition of yttrium(III) propionate and butyrate Thermal decomposition studies of metallorganic compounds View project Substrates for coated conductors View project, Artic. J. Anal. Appl. Pyrolysis. (2013). doi:10.1016/j.jaap.2013.01.011.

[22] M. Nasui, R.B. Mos, T. Petrisor Jr, M.S. Gabor, R.A. Varga, L. Ciontea, T. Petrisor, Synthesis, crystal structure and thermal decomposition of a new copper propionate [Cu (CH3CH2COO) 2]·2H2O, J. Anal. Appl. Pyrolysis. 92 (2011) 439–444.

[23] R.B. Mos, M. Nasui, T. Petrisor Jr, M.S. Gabor, R. Varga, L. Ciontea, T. Petrisor, Synthesis, crystal structure and thermal decomposition study of a new barium acetato-propionate complex, J. Anal. Appl. Pyrolysis. 92 (2011) 445–449.

[24] L. Piperno, A.A. Armenio, A. Vannozzi, A. Mancini, F. Rizzo, A. Augieri, V. Pinto, A. Rufoloni, R.B. Mos, L. Ciontea, others, Polymer-assisted surface decoration for critical current enhancement in \ch{YBa2Cu3O$_{7-x}$}- x films, Appl. Surf. Sci. 484 (2019) 237–244.

[25] O.C. Bridgeman, E.W. Aldrich, Vapor pressure tables for water, J. Heat Transfer. 86 (1964) 279–286. doi:10.1115/1.3687121.

[26] W. Mallard, P.L.- Gaithersburg, undefined MD, undefined 2000, NIST Chemistry WebBook, NIST Standard Reference Database Number 69, (n.d.).

[27] M. Wojdyr, Fityk: A general-purpose peak fitting program, J. Appl. Crystallogr. 43 (2010) 1126–1128. doi:10.1107/S0021889810030499.

[28] R. Svoboda, J. Málek, Applicability of Fraser-Suzuki function in kinetic analysis of complex crystallization processes, J. Therm. Anal. Calorim. 111 (2013) 1045–1056. doi:10.1007/s10973-012-2445-9.

[29] V. Pinto, R. Lamanna, A. Vannozzi, A. Angrisani Armenio, G. De Marzi, A. Augieri, L. Piperno, G. Sotgiu, G. Celentano, Solution Refining for MOD-YBCO Optimization: An NMR Study, IEEE Trans. Appl. Supercond. 28 (2018). doi:10.1109/TASC.2018.2800767.

[30] Z. Li, M. Coll, B. Mundet, A. Palau, T. Puig, X. Obradors, Accelerated growth by flash heating of high critical current trifluoroacetate solution derived epitaxial superconducting \ch{YBa2Cu3O$_{7-x}$} films, J. Mater. Chem. C. 7 (2019) 4748–4759.

[31] A. Angrisani Armenio, A. Augieri, L. Ciontea, G. Contini, I. Davoli, M. Di Giovannantonio, V. Galluzzi, A. Mancini, A. Rufoloni, T. Petrisor, others, Structural and chemical evolution of propionate based metal--organic precursors for superconducting \ch{YBa2Cu3O$_{7-x}$} epitaxial film growth, Supercond. Sci. Technol. 24 (2011) 115008.

[32] M. Yoshizumi, I. Seleznev, M.J. Cima, Reactions of oxyfluoride precursors for the preparation of barium yttrium cuprate films, Phys. C Supercond. Its Appl. 403 (2004) 191–199. doi:10.1016/j.physc.2003.12.004.

[33] R.P. Vasquez, M.C. Foote, B.D. Hunt, Reaction of nonaqueous halogen solutions with YBa2Cu3O7- x, J. Appl. Phys. 66 (1989) 4866–4877.

[34] A. Tressaud, K. Amine, J.P. Chaminade, J. Etourneau, T.M. Duc, A. Sartre, X-ray photoelectron spectroscopy study of fluorine-treated YBa2Cu3O7- $δ$ crystals, J. Appl. Phys. 68 (1990) 248–254.

[35] J.H. Su, P.P. Joshi, V. Chintamaneni, S.M. Mukhopadhyay, Photoelectron spectroscopic investigation of transformation of trifluoroacetate precursors into superconducting YBa2Cu3O7- $δ$ films, Appl. Surf. Sci. 253 (2007) 4652–4658.

[36] A. Gauzzi, H.J. Mathieu, J.H. James, B. Kellett, AES, XPS and SIMS characterization of YBa2Cu3O7 superconducting high Tc thin films, Vacuum. 41 (1990) 870–874.

[37] G. Schön, ESCA studies of Cu, Cu2O and CuO, Surf. Sci. 35 (1973) 96–108.

[38] Z. Hussain, M.A. Salim, M.A. Khan, E.E. Khawaja, X-ray photoelectron and auger spectroscopy study of copper-sodium-germanate glasses, J. Non. Cryst. Solids. 110 (1989) 44–52.

[39] M.P. Seah, D. Briggs, Practical Surface Analysis: Auger and X-ray Photoelectron Spectroscopy, John Wiley & Sons, 1990.

[40] D. Majumdar, D. Chatterjee, X-ray photoelectron spectroscopic studies on yttria, zirconia, and yttria-stabilized zirconia, J. Appl. Phys. 70 (1991) 988–992.

[41] S. Youngme, A. Cheansirisomboon, … C.D.-I.C., undefined 2008, Polynuclear paddle-wheel copper (II) propionate with di-2-pyridylamine or 1, 10-phenanthroline: Preparation, characterization and X-ray structure, Elsevier. (n.d.). https://www.sciencedirect.com/science/article/pii/S1387700307003668 (accessed December 10, 2019).

[42] H. Eloussifi, J. Farjas, P. Roura, S. Ricart, T. Puig, X. Obradors, M. Dammak, Thermal decomposition of barium trifluoroacetate thin films, Thermochim. Acta. 556 (2013) 58–62.

[43] R.L. Tischer, G. Burner, Preparation of yttrium flouride using fluorine, 1959. http://lib.dr.iastate.edu/ameslab_isreports/8 (accessed December 10, 2019).

[44] A. Mukherjee, A. Awasthi, S. Mishra, N.K.-T. Acta, undefined 2011, Studies on fluorination of Y2O3 by NH4HF2, Elsevier. (n.d.). https://www.sciencedirect.com/science/article/pii/S0040603111002139 (accessed December 10, 2019).

[45] P. Roura, J. Farjas, H. Eloussifi, L. Carreras, S. Ricart, T. Puig, X. Obradors, Thermal analysis of metal organic precursors for functional oxide preparation: Thin films versus powders, Thermochim. Acta. 601 (2015) 1–8. doi:10.1016/j.tca.2014.12.016.

Supporting info

Characterization of the single precursors

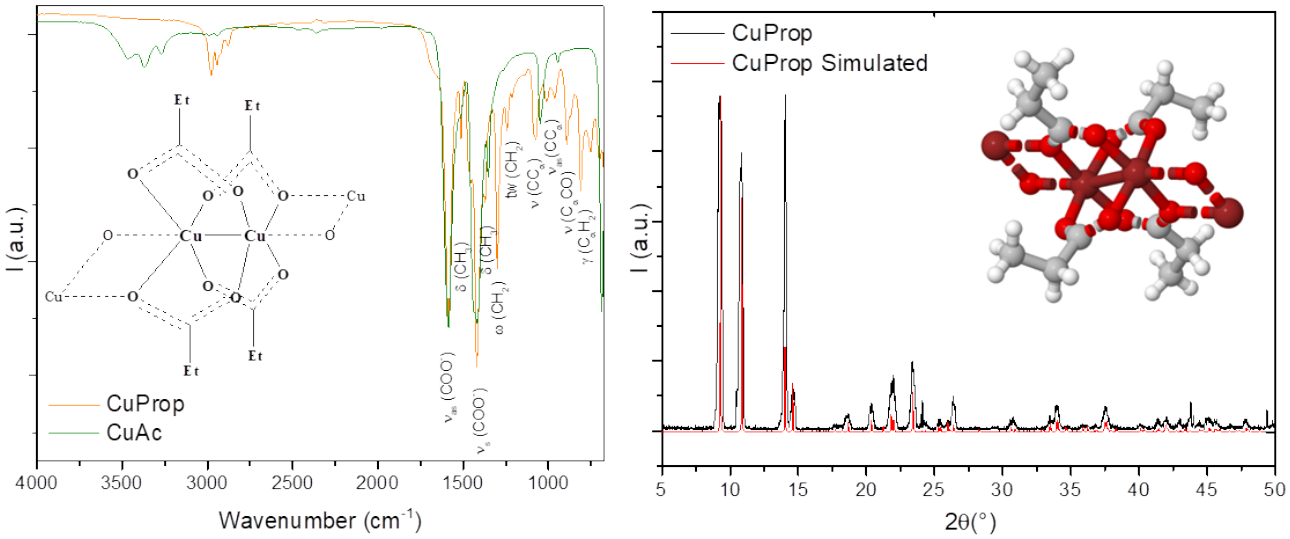

Fig. S1: On the left: FTIR spectra of copper acetate and the precipitate obtained from the solution, identified as copper propionate; on the right, comparison between the X-ray diffraction pattern of the precipitate compared with the simulated spectra of copper propionate CCDC database code 1133510.

***Copper Acetate*:** Both the commercial powder and the precipitate obtained from the solution of copper acetate in propionic acid were analysed. The superposition of the IR spectra of both species in fig 1 reveal the appearance, in the precipitate, of a large number of peaks in the region of the skeletal vibrations of the molecule. This behaviour is consistent with the ligand exchange between acetate and propionate ions in the solution that lead to the formation of the new compound copper propionate ($CuProp_2$). Also, comparison with reference spectra from the literature identifies the precipitate as $CuProp_2$. XRD diffraction performed on the powder gave further insight of the system. Perfect match of the experimental data is found with the structure from CCDC database code 1133510, that consists of a polinuclear structure of $CuProp_2$ in which additional bonds are formed between the copper atoms and the counter ions behave as bridges between the two metallic nuclei. From this information we can confirm the hypothesis of ligand exchange in the solution with the subsequent elimination of the acetate counter ions already at 80°C.

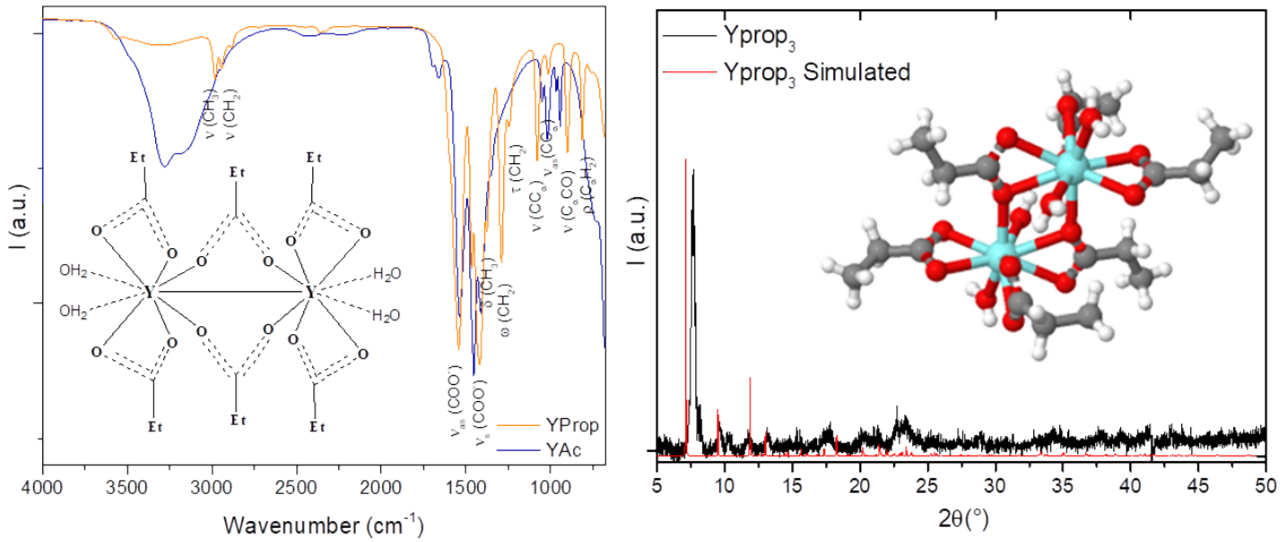

Fig. S2: On the left: FTIR spectra of yttrium acetate and the precipitate obtained from the solution, identified as yttrium propionate; on the right, comparison between the X-ray diffraction pattern of the precipitate compared with the simulated spectra of yttrium propionate CCDC database code 873618.

Yttrium Acetate: The same behaviour is observed with yttrium acetate in propionic acid. Both IR and XRD measurements confirm the formation of $YProp_3$. The structure of the compound is similar to that of $CuProp_2$. A binuclear structure is formed in which two Y^{3+} atoms are bound by six propionate counter ions, two of which behave as bridges between the two metallic centres. A slight difference in the XRD experimental vs simulated spectra can be explained with a different hydration of the compound.

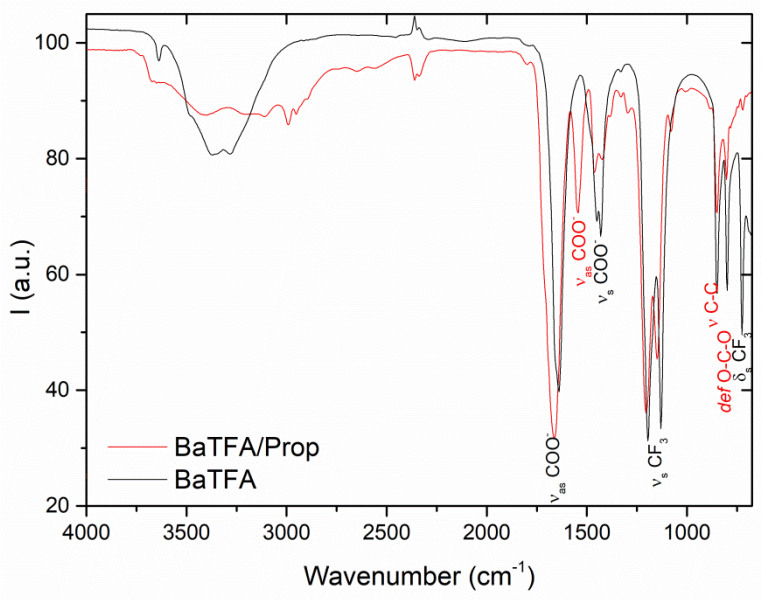

Fig. S3: FTIR spectra of barium trifluoroacetate and the precipitate obtained from the solution, identified as a mixed species of barium trifluoroacetate/propionate.

***Barium Trifluoroacetate*:** From the IR spectrum of the powder, instead, the presence of also a mixed species like BaTFA(Prop) of unknown stoichiometry was detected from the coexistence of signals belonging to both ligands, therefore this will be considered as the precursor together with BaTFA. In our case, the XRD analysis of the could not give a clear match to a known structure of $BaProp_x$ and no reference to a mixed TFA/propionate species was found in the literature.

Evolved Gas Analysis

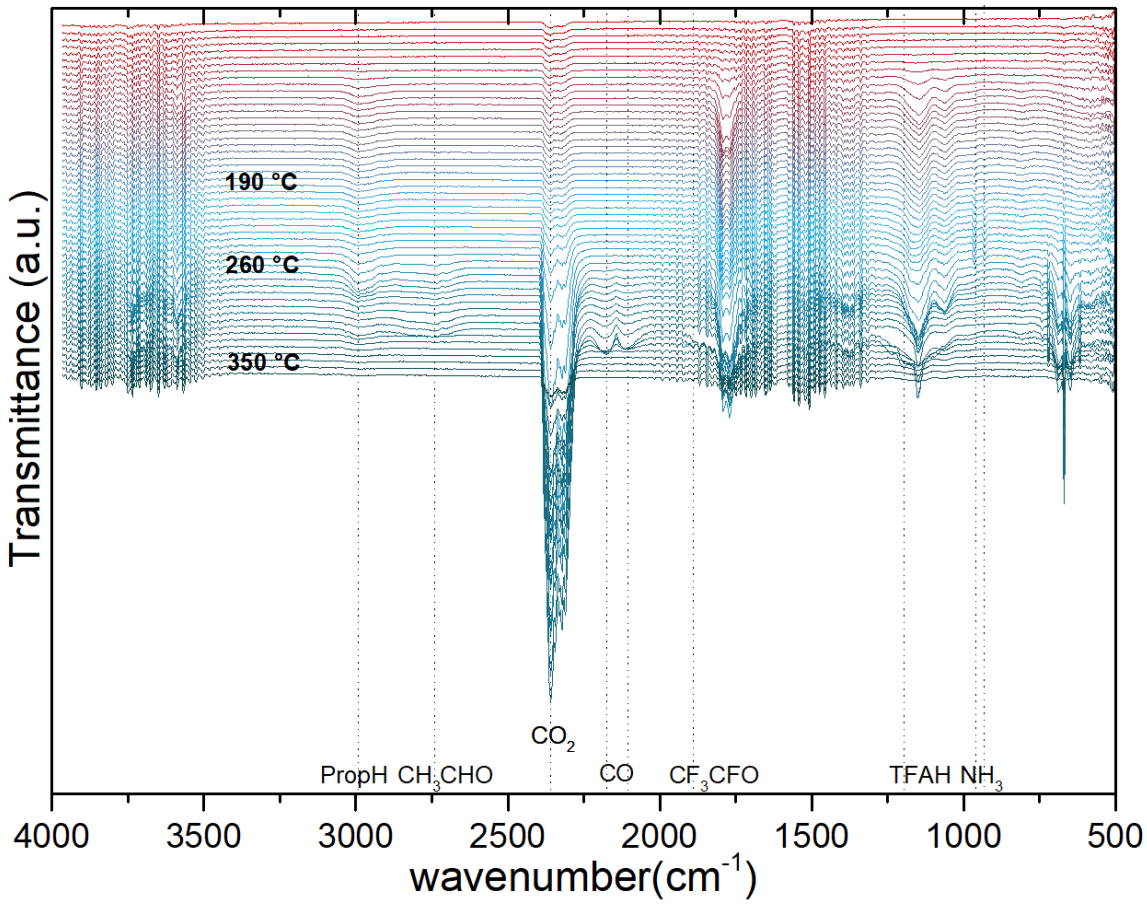

Fig. S4: EGA analysis of the precursor solution. For clarity, one third of the obtained spectra is plotted. The frequencies used to extrapolate the gas evolution curves are marked with dotted lines. Three labels help to visualize the temperature range in which the processes occur.

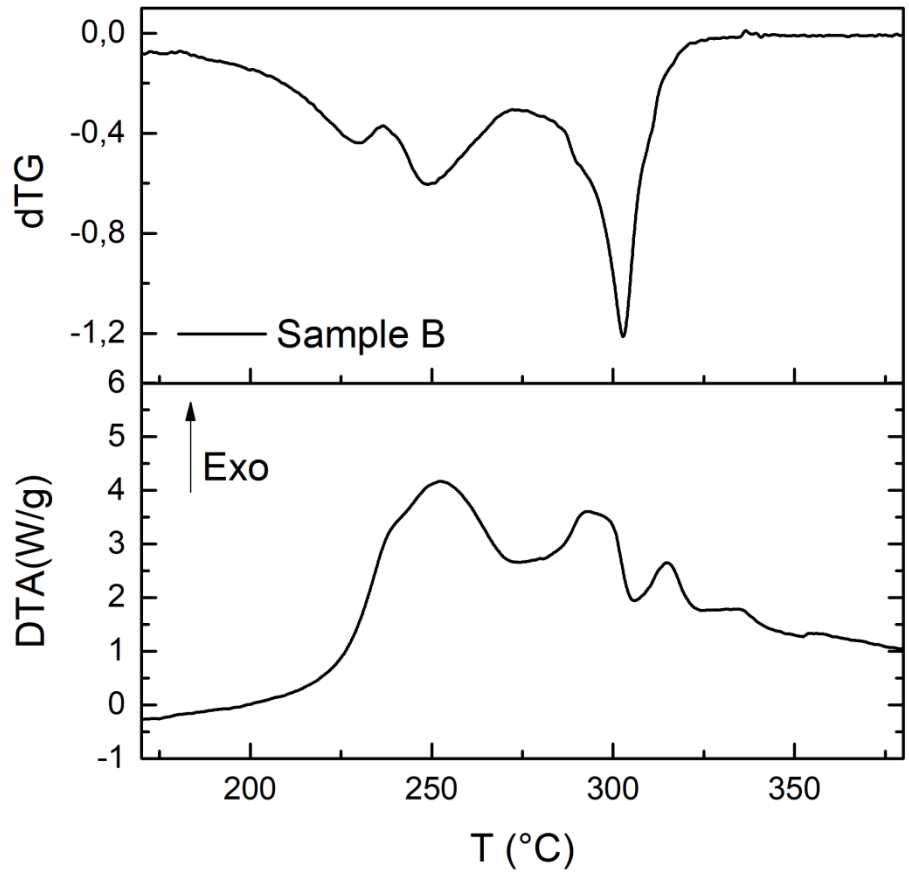

Fig. S5: dTG and DSC measurements performed on sample C showing the exothermic peaks typical of the oxidative mechanism involved in the pyrolysis process.

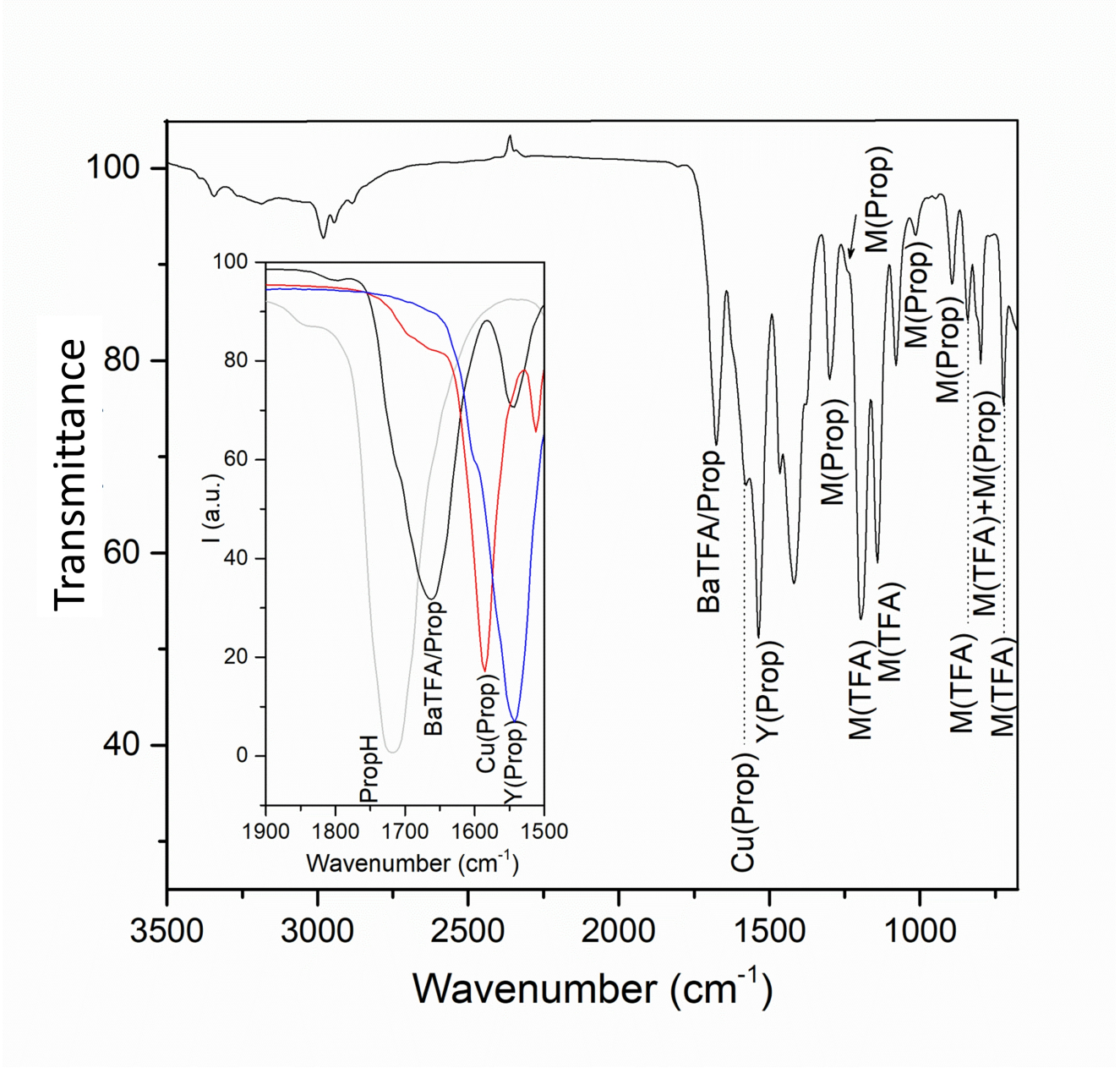
Transmittance
100
80
60
40
3500
3000
2500
2000
1500
1000
Wavenumber (cm-1)
BaTFA/Prop
Cu(Prop)
Y(Prop)
M(Prop)
M(TFA)
M(TFA)
M(Prop)
M(Prop)
M(Prop)
M(TFA)
M(TFA)+M(Prop)
M(TFA)
I (a.u.)
100
80
60
40
20
0
1900
1800
1700
1600
1500
Wavenumber (cm-1)
PropH
BaTFA/Prop
Cu(Prop)
Y(Prop)

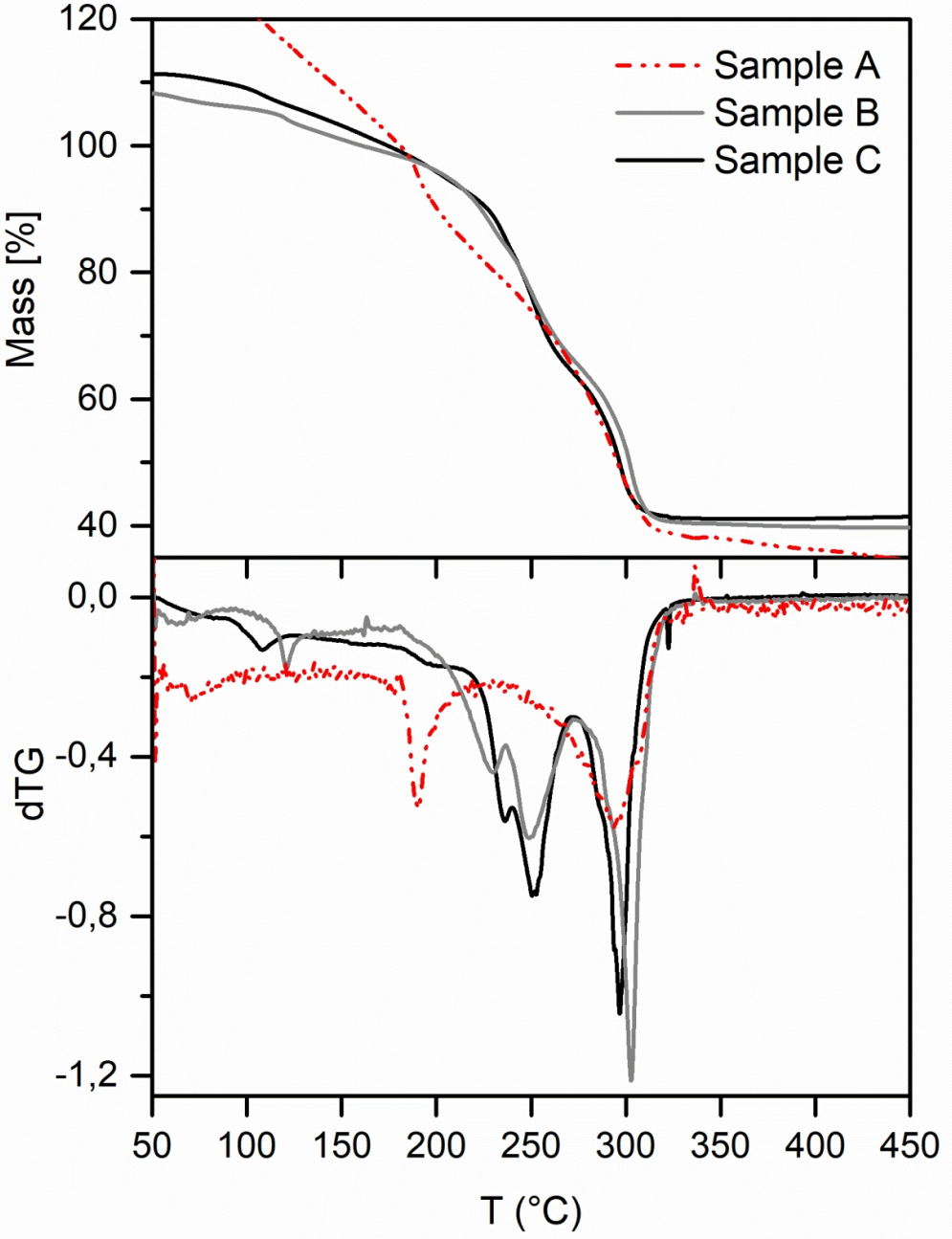
Sample A
Sample B
Sample C
Mass [%]
120
100
80
60
40
dTG
0,0
-0,4
-0,8
-1,2
50
100
150
200
250
300
350
400
450
T (°C)

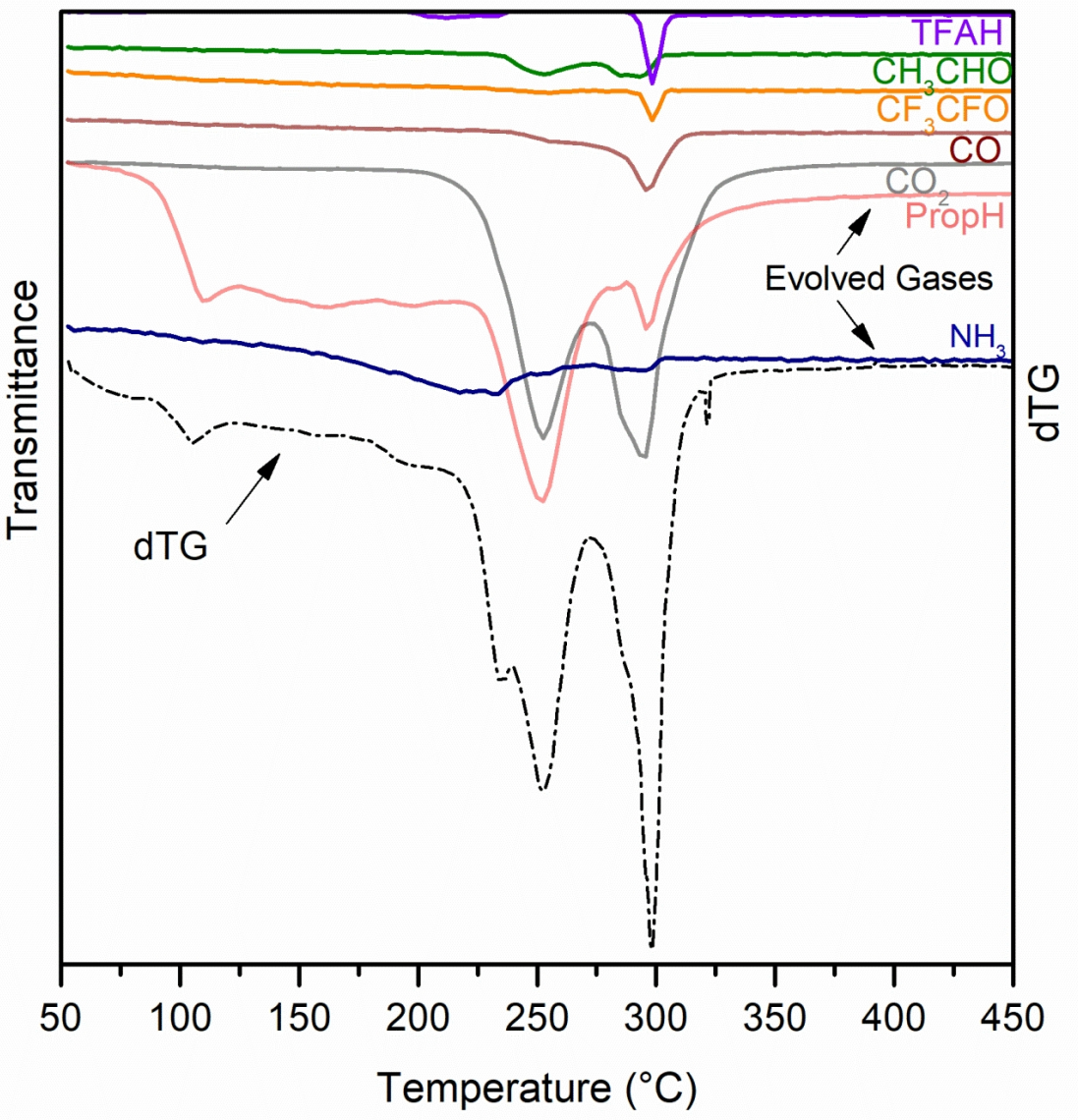
TFAH
CH3CHO
CF3CFO
CO
CO2
PropH
Evolved Gases
NH3
dTG
Transmittance
dTG
50
100
150
200
250
300
350
400
450
Temperature (°C)

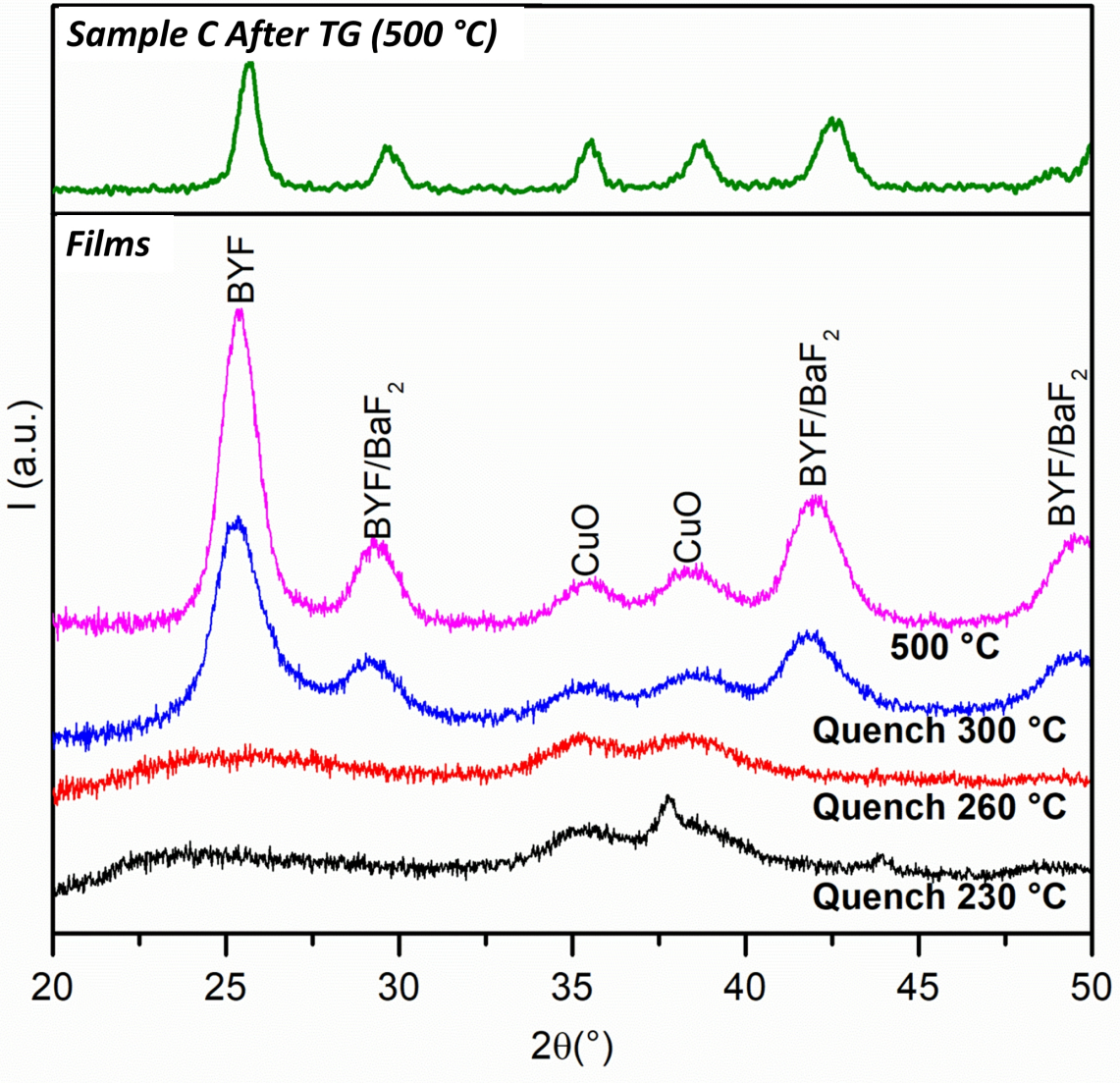
Sample C After TG (500 °C)
Films
BYF
BYF/BaF2
CuO
CuO
BYF/BaF2
BYF/BaF2
500 °C
Quench 300 °C
Quench 260 °C
Quench 230 °C
I (a.u.)
20
25
30
35
40
45
50
2θ(°)

Sample C after TA (500 °C)

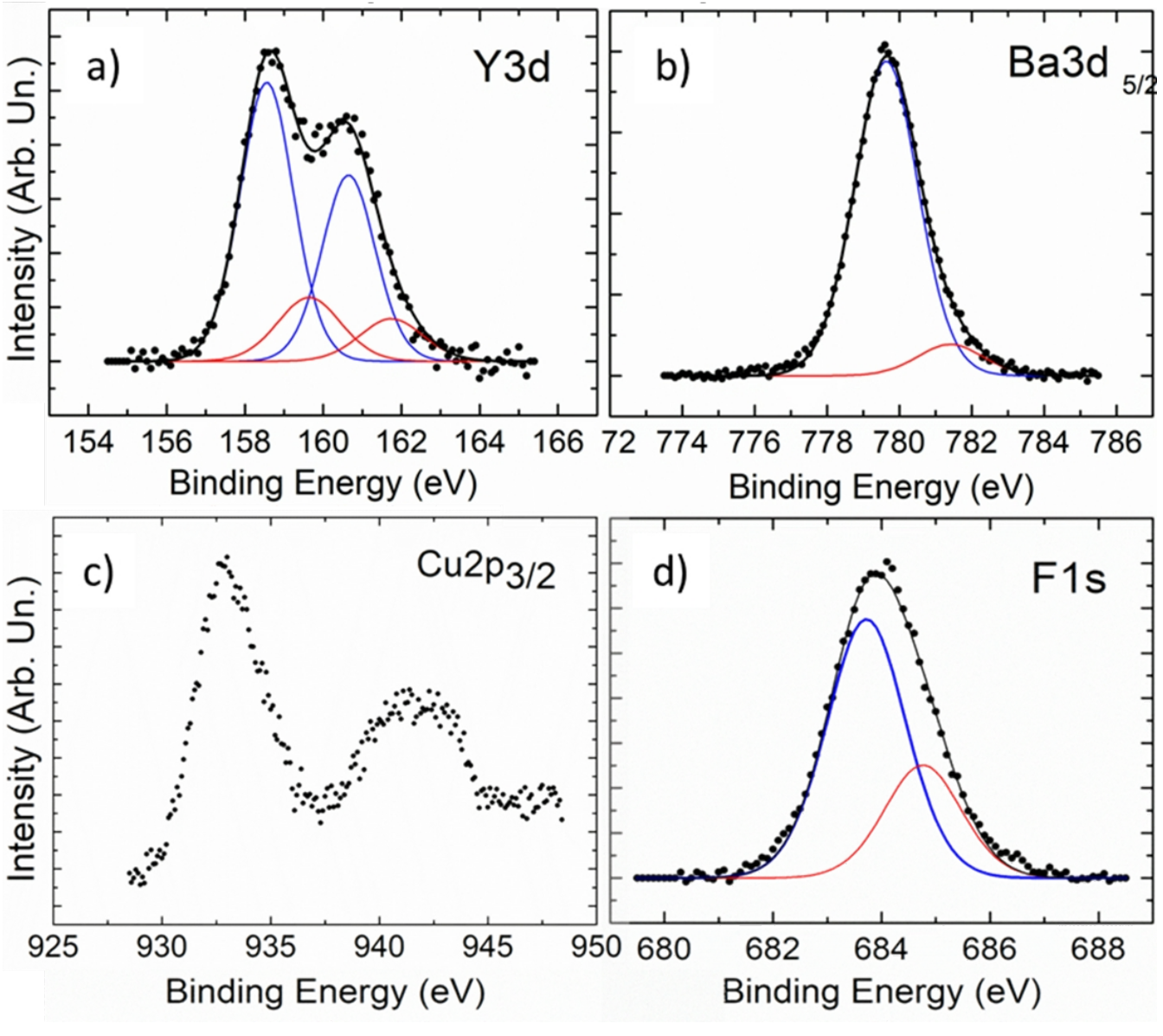

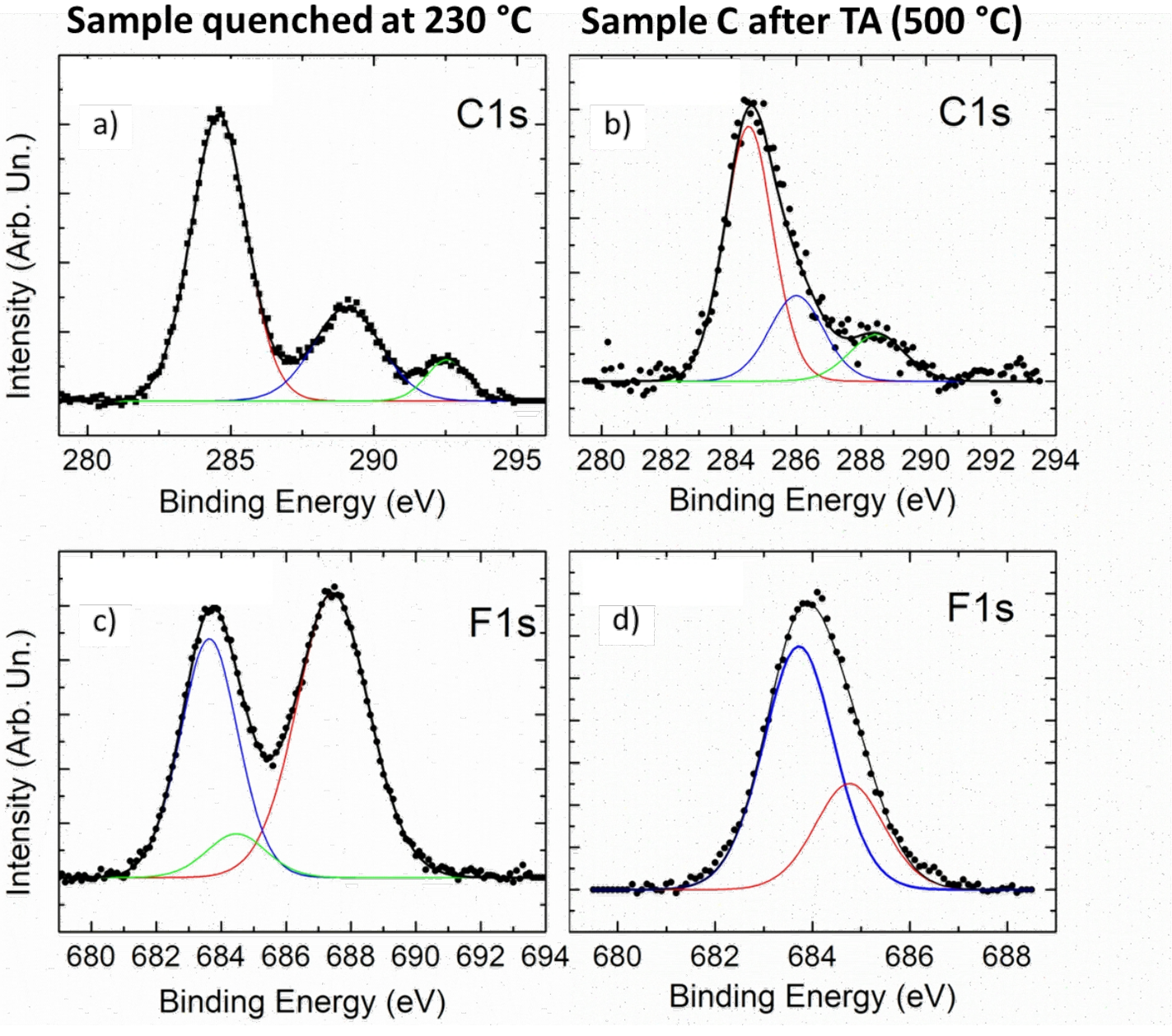
Sample quenched at 230 °C
Sample C after TA (500 °C)
a)
C1s
b)
C1s
c)
F1s
d)
F1s
Intensity (Arb. Un.)
Intensity (Arb. Un.)
280 285 290 295
Binding Energy (eV)
280 282 284 286 288 290 292 294
Binding Energy (eV)
680 682 684 686 688 690 692 694
Binding Energy (eV)
680 682 684 686 688
Binding Energy (eV)

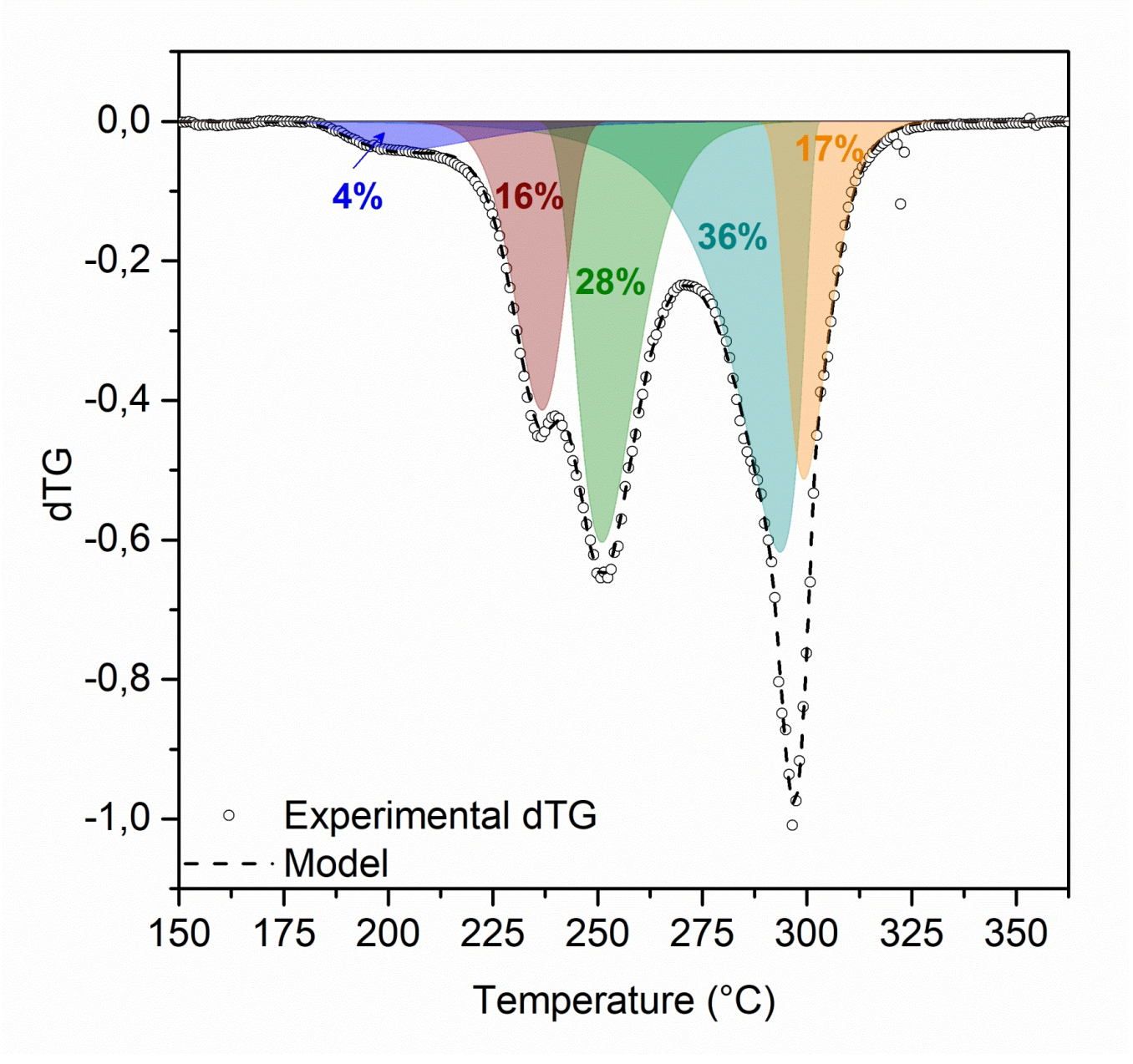
0,0
-0,2
-0,4
-0,6
-0,8
-1,0
dTG
4%
16%
28%
36%
17%
Experimental dTG
Model
150
175
200
225
250
275
300
325
350
Temperature (°C)

Declaration of interests

 The authors declare that they have no known competing financial interests or personal relationships that could have appeared to influence the work reported in this paper.

☐The authors declare the following financial interests/personal relationships which may be considered as potential competing interests:

Supporting info

Characterization of the single precursors

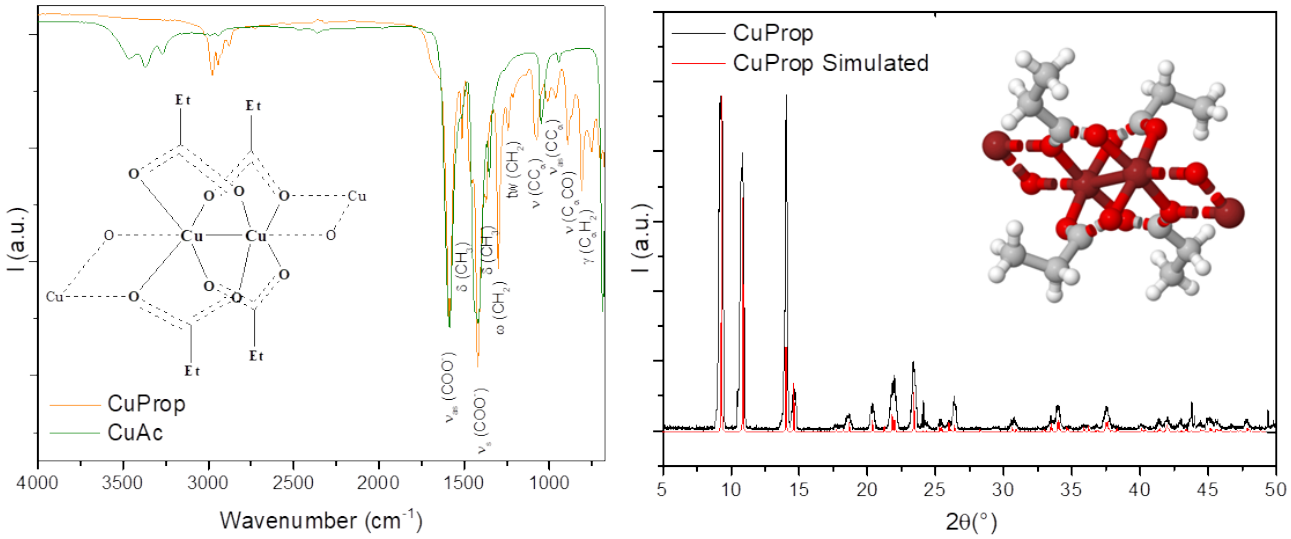

Fig. S1: On the left: FTIR spectra of copper acetate and the precipitate obtained from the solution, identified as copper propionate; on the right, comparison between the X-ray diffraction pattern of the precipitate compared with the simulated spectra of copper propionate CCDC database code 1133510.

***Copper Acetate*:** Both the commercial powder and the precipitate obtained from the solution of copper acetate in propionic acid were analysed. The superposition of the IR spectra of both species in fig 1 reveal the appearance, in the precipitate, of a large number of peaks in the region of the skeletal vibrations of the molecule. This behaviour is consistent with the ligand exchange between acetate and propionate ions in the solution that lead to the formation of the new compound copper propionate ($CuProp_2$). Also, comparison with reference spectra from the literature identifies the precipitate as $CuProp_2$. XRD diffraction performed on the powder gave further insight of the system. Perfect match of the experimental data is found with the structure from CCDC database code 1133510, that consists of a polinuclear structure of $CuProp_2$ in which additional bonds are formed between the copper atoms and the counter ions behave as bridges between the two metallic nuclei. From this information we can confirm the hypothesis of ligand exchange in the solution with the subsequent elimination of the acetate counter ions already at 80°C.

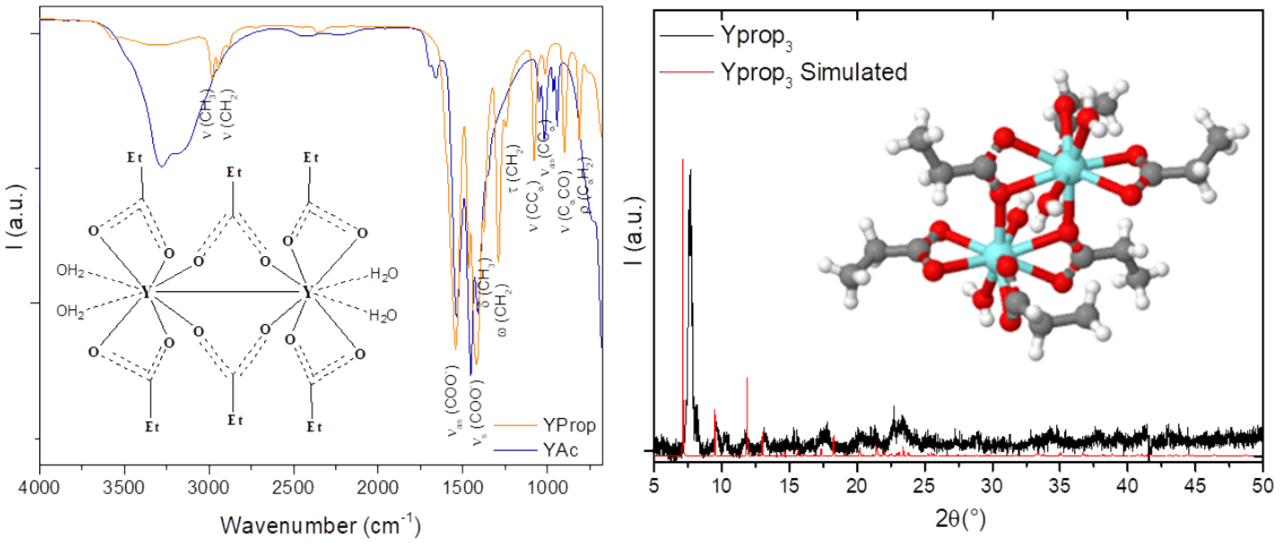

Fig. S2: On the left: FTIR spectra of yttrium acetate and the precipitate obtained from the solution, identified as yttrium propionate; on the right, comparison between the X-ray diffraction pattern of the precipitate compared with the simulated spectra of yttrium propionate CCDC database code 873618.

Yttrium Acetate: The same behaviour is observed with yttrium acetate in propionic acid. Both IR and XRD measurements confirm the formation of $YProp_3$. The structure of the compound is similar to that of $CuProp_2$. A binuclear structure is formed in which two Y^{3+} atoms are bound by six propionate counter ions, two of which behave as bridges between the two metallic centres. A slight difference in the XRD experimental vs simulated spectra can be explained with a different hydration of the compound.

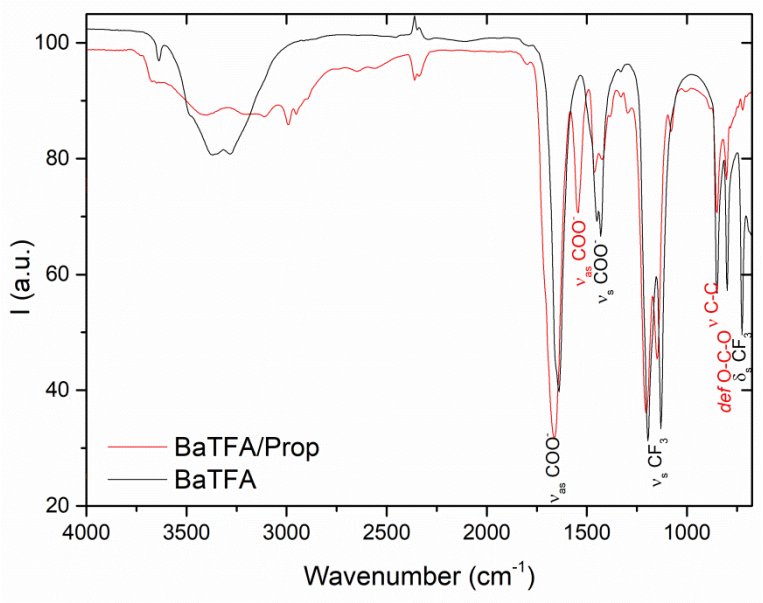

Fig. S3: FTIR spectra of barium trifluoroacetate and the precipitate obtained from the solution, identified as a mixed species of barium trifluoroacetate/propionate.

***Barium Trifluoroacetate*:** From the IR spectrum of the powder, instead, the presence of also a mixed species like BaTFA(Prop) of unknown stoichiometry was detected from the coexistence of signals belonging to both ligands, therefore this will be considered as the precursor together with BaTFA. In our case, the XRD analysis of the could not give a clear match to a known structure of $BaProp_x$ and no reference to a mixed TFA/propionate species was found in the literature.

Evolved Gas Analysis

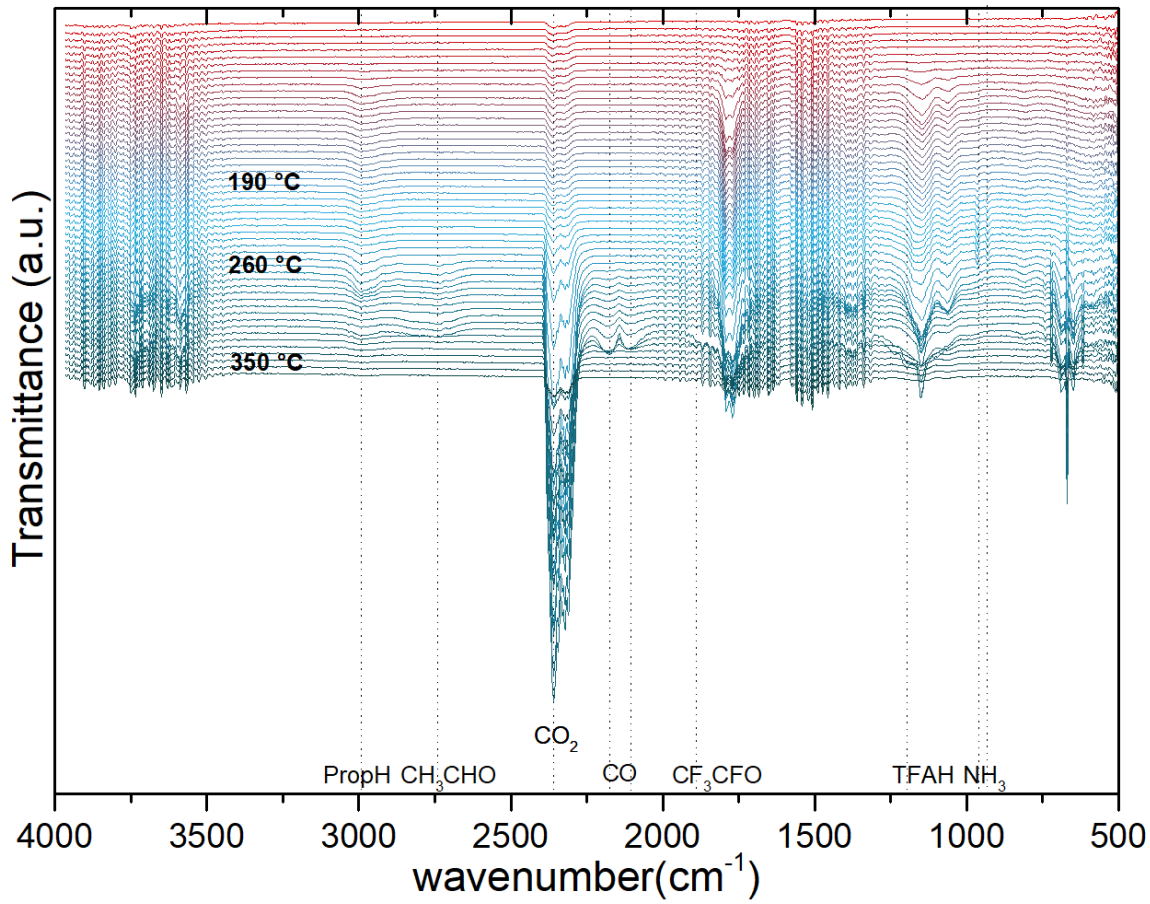

Fig. S4: EGA analysis of the precursor solution. For clarity, one third of the obtained spectra is plotted. The frequencies used to extrapolate the gas evolution curves are marked with dotted lines. Three labels help to visualize the temperature range in which the processes occur.

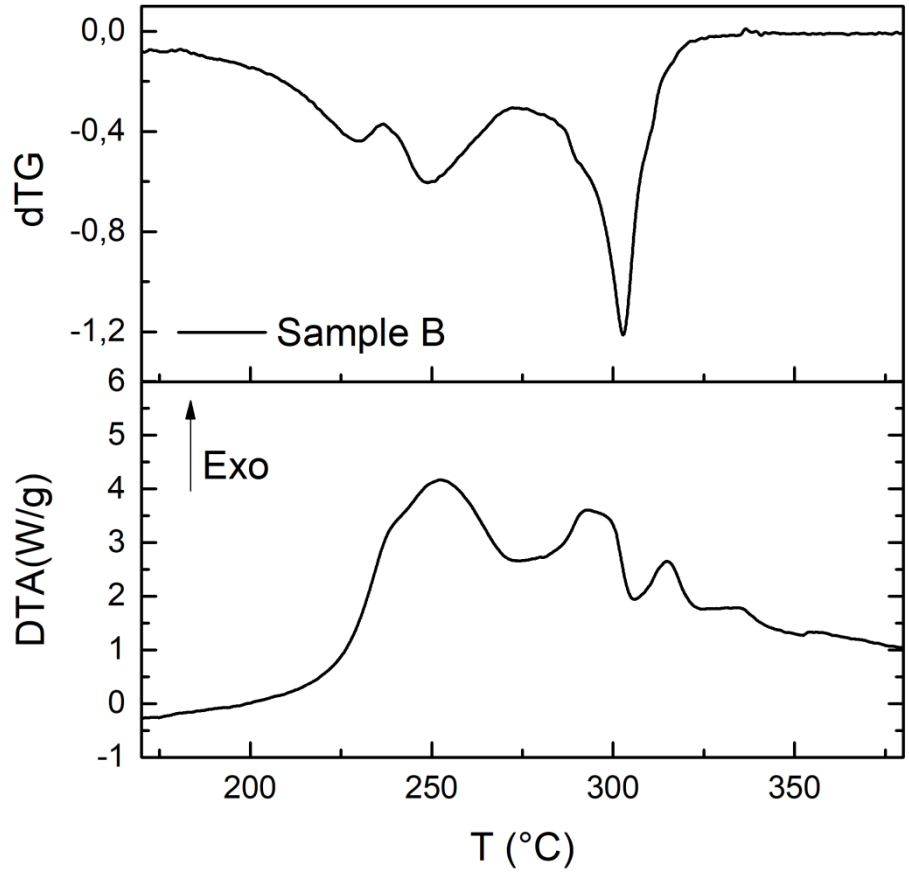

Fig. S5: dTG and DSC measurements performed on sample C showing the exothermic peaks typical of the oxidative mechanism involved in the pyrolysis process.